3-24-2016

Using Phase Screens To Synthesize Electromagnetic Gaussian-Schell Model Sources With Desired Amplitude, Coherence, and Polarization

Christopher K. Kokoczka

USING PHASE SCREENS TO SYNTHESIZE ELECTROMAGNETIC GAUSSIAN-SCHELL MODEL SOURCES WITH DESIRED AMPLITUDE, COHERENCE, AND POLARIZATION

THESIS

Christopher J. Kokoczka, Capt, USAF

AFIT-ENG-MS-16-M-026

DEPARTMENT OF THE AIR FORCE
AIR UNIVERSITY

AIR FORCE INSTITUTE OF TECHNOLOGY

Wright-Patterson Air Force Base, Ohio

AFIT-ENG-MS-16-M-026

USING PHASE SCREENS TO SYNTHESIZE ELECTROMAGNETIC GAUSSIAN-SCHELL MODEL SOURCES WITH DESIRED AMPLITUDE, COHERENCE, AND POLARIZATION

THESIS

Presented to the Faculty

Department of Electrical and Computer Engineering

Graduate School of Engineering and Management

Air Force Institute of Technology

Air University

Air Education and Training Command

in Partial Fulfillment of the Requirements for the

Degree of Master of Science in Electrical Engineering

Christopher J. Kokoczka, B.S.E.E.

Capt, USAF

24 March 2016

AFIT-ENG-MS-16-M-026

USING PHASE SCREENS TO SYNTHESIZE ELECTROMAGNETIC GAUSSIAN-SCHELL MODEL SOURCES WITH DESIRED AMPLITUDE, COHERENCE, AND POLARIZATION

THESIS

Christopher J. Kokoczka, B.S.E.E.
Capt, USAF

Committee Membership:

Maj Milo Hyde
Chair

Dr. Santasri Basu
Member

Dr. Steve Fiorino
Member

Abstract

An electromagnetic Gaussian-Schell model (EGSM) source is built with desired coherence, amplitude, and polarization using correlated phase screens based on research conducted in Refs. [2, 9]. A new method of amplitude control is presented and tested using spatial light modulators (SLM). A brief review of theory and concepts is discussed followed by methods of how to build an EGSM source, correlated phase screens, and control amplitude using SLM gratings. The experimental set-up is presented which builds EGSM sources that demonstrate desired amplitude, coherence, and polarization. Irradiance correlation, degree of polarization, and Stokes parameters S_0 and S_1 are examined and compared to theoretical predictions to validate experimental results. The results are summarized and future work is discussed including methods of calculating and measuring Stokes S_2 and S_3.

Acknowledgements

I would like to thank my family and friends for supporting me and being there with me along this journey. They have always encouraged me to strive and expand my knowledge and understanding of the world, as well as to challenge myself. A special thanks goes out to my research advisor Major Milo Hyde and mentors Dr. Santasri Basu and Dr. Jack McCrae. Without their patience, instruction, and investment, I would never have seen the light!

Christopher J. Kokoczka

Table of Contents

Page

List of Abbreviations

Abbreviation		Page
EGSM	electromagnetic Gaussian-Schell model	iv
GSM	Gaussian-Schell model	1
SLM	spatial light modulators	1
AFIT	Air Force Institute of Technology	1
OPD	optical path difference	3
MCF	mutual coherence function	5
CDoC	complex degree of coherence	6
CSD	cross-spectral density	6
SDoC	spectral degree of coherence	6
CSDM	cross-spectral density matrix	8
DoP	degree of polarization	9
AoP	angle of polarization	10
BE	beam expander	11
HWP	half-wave plate	11
LP	linear polarizer	11
PBS	polarized beam splitter	11
LS	lens system	12
JCF	joint characteristic function	16
FOCF	fourth-order correlation function	30
GAF	Gaussian amplitude filter	43
EBGSM	electro-magnetic Bessel-Gaussian Schell model beams	48
VR	variable retarder	48

List of Figures

List of Tables

USING PHASE SCREENS
TO SYNTHESIZE ELECTROMAGNETIC GAUSSIAN-SCHELL MODEL
SOURCES WITH DESIRED AMPLITUDE, COHERENCE, AND
POLARIZATION

I. Introduction

There has been substantial amounts of research conducted on electromagnetic Gaussian-Schell model EGSM sources in the last two decades [2, 15]. This class of source beams is ideal for studying as many properties of Gaussians are preserved during propagation making an observable connection between source beam parameters and observation irradiance measurements. Most research has focused on scalar Gaussian-Schell model (GSM) beams, and only recently has the model been expanded to explore vector sources due to polarimetric changes that occur during propagation. In order to effectively model EGSMs, one needs a partially coherent and partially polarized source with well known statistical properties. Since the most common source in a lab environment is a laser, whose radiation is almost completely coherent and polarized, realization of EGSMs has existed mostly in computer simulations and models. Now, due to the availability of spatial light modulators (SLM), which can alter the phase of incoming sources, constructing EGSMs in a lab environment has become more practical [8, 13, 15].

In 2015, an experiment was conducted described in Ref. [9] at the Air Force Institute of Technology (AFIT). The experiment demonstrated that an EGSM beam could be created with desired coherence and polarization properties by commanding two SLMs to control phases for both the E_x and E_y field components. However, the range

of EGSM sources that could be produced was limited because of the experimental set-up. There were also complications with validating the desired polarization state of the propagated beam, particularity Stokes parameters S_2 and S_3.

The appeal and necessity for controlling amplitude, coherence, and polarization is ideal for many laser applications as the desired result is to place as much energy on a target with minimal loss in transmitted power. The correlation between all three parameters can influence the total power received or information that can be transmitted. For vector beams, the power in $|E_x|^2$ plus $|E_y|^2$ is the total power present. Coherence can influence the amplitude by its constructive and destructive properties both spatially and temporally; in a vacuum the more coherent the beam, the more correlated the beam is spatially and temporally. Finally coherence can influence polarization in the transverse plan between E_x and E_y. As the coherence in both orthogonal planes increases, the degree of polarization also increases. This is further influenced by the fact that cross correlation and polarization can evolve during propagation. Thus controlling all three parameters can greatly influence the observed beam in the observation plane.

Through continuation of work conducted in Ref. [2, 9], an EGSM source with desired amplitude, coherence, and polarization will be made. In the process of making an EGSM source, new techniques for over all optical train footprint reduction, measuring polarization, and controlling amplitude will be explored and validated. The anticipated result will be more control, an easier experimental set-up, and increased accuracy in measured results compared to previous methods and research.

1.1. Report Objectives

The objective of the research is built on further expansion of the research conducted in Ref. [2, 9]. The overall goal is to effectively generate an EGSM source with

desired coherence, amplitude, and polarization. However, the methods and design have been changed to add more flexibility and control to the experiment. There are three main focus area addressed in this research effort:

1. Control EGSM amplitude with the SLMs via commanded grating. The anticipated effect of this will be another controllable beam characteristic as opposed to fixed optical elements controlling overall amplitude.

2. Reduce registration errors by eliminating optical elements and mechanical adjustments taken during polarization measurements. Achieving amplitude control via the SLMs will already reduce optical elements. In addition, through a new polarimeter design, S_0 and S_1 will be measured simultaneously on the same camera through spatially separated irradiance measurements.

3. Effectively measure polarization and Stokes parameters by using a redesigned polarimeter.

1.2. Limitations

Many variables are involved with the generation of an EGSM source experimentally. Some challenges that will govern the accuracy and thoroughness of this experiment are time and equipment on hand. Although efforts have been made to mitigate ambient light and table vibration; there are still random contributions from vibration and thermal changes that can influence the optical path difference (OPD); which can contaminate measured results. These errors were present and documented in previous experiments [9]. Furthermore, despite a new polarimeter design, Stokes parameters S_2 and S_3 cannot be measured. During preliminary testing and design of a four camera polarimeter that measured four simultaneous irradiance patterns to create a Stokes vector, it was discovered that OPD lengths of both the E_x and E_y

legs varied randomly. This random oscillation makes measuring a circular, elliptical, and $+45°/-45°$ state difficult as the rotation can vary with any given instance. Refer to Chapter 5 which has recommendations for addressing this issue in future work.

1.3. Implications

Results from this research have far reaching potential to further research, development, and implementation in the areas of optical communications, imaging through turbulence, remote sensing, and directed energy applications. Of further note, is the ability to simplify the process of creating EGSMs in a lab and validate what was once limited only to theory due to the complexity of the experimental design. Through further advancements in SLM design and optical elements, and by furthering polarization analysis, potential exists for future development and control of EGSM parameters or other beam shapes.

1.4. Preview

The experimental research presented in this document aims to demonstrate that an EGSM source can be generated with desired coherence, amplitude, and polarization with the amplitude being controlled by an applied grating on the SLM. Chapter 2, the Literature Review, discusses previous research and fundamental mathematical concepts that are key and routinely used in the design of the theory and experiment. Chapter 3, Methodology, details the computational methods of creating a correlated EGSM source, controlling amplitude with the SLM, the physical layout of the lab bench, and how results are measured and calculated. Chapter 4, Analysis and Results, interprets the gathered theoretical, simulated, and experimental data. Chapter 5, Conclusions and Recommendations, discusses the validity and performance of the experiment and provides recommendations for future research areas.

II. Background Concepts and Theory

All optical fields undergo random fluctuations. They can be small, as with a many lasers, or they can be large, as with thermal sources. The area of study that describes these fluctuations is known as coherence theory. Chapter 2 discusses the theory behind coherence and polarization and how they are used in the propagation of EGSM beams.

2.1. Coherence

In a given random field, coherence describes the degree to which one point relates to any other point in the field in time or space. More specifically, it refers to how a wave interferes with itself. Coherence is realized mathematically through the correlation function $\Gamma(\boldsymbol{r_1}, \boldsymbol{r_2}; t_1, t_2)$. The correlation function Γ depends on two points in the field space $(\boldsymbol{r_1}, \boldsymbol{r_2})$ or two instances in time (t_1, t_2).

2.1.1 Mutual coherence function.

The mutual coherence function (MCF) $\Gamma(\boldsymbol{r_1}, \boldsymbol{r_2}; \tau)$ is used in second order statistics to analyze spatial coherence [6, 22] where,

$$\Gamma(\boldsymbol{r_1}, \boldsymbol{r_2}; \tau) = \langle U(\boldsymbol{r_1}, t+\tau) U^*(\boldsymbol{r_2}, t) \rangle \tag{1}$$

Equation 1 is the time auto correlation of an analytical function $u(r, t)$ at two points in space $\boldsymbol{r_1}$ and $\boldsymbol{r_2}$. If $\boldsymbol{r_1} = \boldsymbol{r_2}$ then Eq. (1) reduces to the self-coherence function. An assumption is made that the field is at least WSS, meaning the average field has no explicit time dependence and the auto-correlation function depends only on the time difference τ.

2.1.2 Complex degree of coherence.

The complex degree of coherence (CDoC) $\gamma(\boldsymbol{r_1}, \boldsymbol{r_2}; \tau)$ is the normalized form of the MCF:

$$\gamma(r_1, r_2, \tau) = \frac{\Gamma(\boldsymbol{r_1}, \boldsymbol{r_2}, \tau)}{\sqrt{\Gamma(\boldsymbol{r_1}, \boldsymbol{r_1}, \tau)\Gamma(\boldsymbol{r_2}, \boldsymbol{r_2}, \tau)}} \tag{2}$$

The magnitude of the CDoC measures the amount of temporal or spatial coherence. The field is considered fully coherent if $|\gamma(\boldsymbol{r_1}, \boldsymbol{r_2}, \tau)| = 1$, fully incoherent if $|\gamma(\boldsymbol{r_1}, \boldsymbol{r_2}, \tau)| = 0$, and partially coherent if $0 < |\gamma(\boldsymbol{r_1}, \boldsymbol{r_2}, \tau)| < 1$.

2.1.3 Cross-spectral density.

It is more convenient to work in the spatial-frequency domain with the cross-spectral density (CSD) function $W(\boldsymbol{r_1}, \boldsymbol{r_2}, \omega)$, as it looks at spectral contribution of each frequency and works for both a broadband and monochromatic source. The CSD and MCF also form a Fourier transform pair such that [22],

$$\begin{aligned} W(\boldsymbol{r_1}, \boldsymbol{r_2}; \omega) &= \langle U(\boldsymbol{r_1}, \omega) U^*(\boldsymbol{r_2}, \omega) \rangle \\ \Gamma(\boldsymbol{r_1}, \boldsymbol{r_2}, \tau) &= \int_{-\infty}^{\infty} W(\boldsymbol{r_1}, \boldsymbol{r_2}, \omega) \exp(\mathrm{j}\omega\tau) d\omega \end{aligned} \tag{3}$$

This is convenient as it forms a space/frequency and time/frequency relation.

2.1.4 Spectral degree of coherence.

Normalizing the CSD in Eq. (3) yields the spectral degree of coherence (SDoC) $\mu(\boldsymbol{r_1}, \boldsymbol{r_2}, \omega)$, where,

$$\mu(\boldsymbol{r_1}, \boldsymbol{r_2}, \omega) = \frac{W(\boldsymbol{r_1}, \boldsymbol{r_2}, \omega)}{\sqrt{W(\boldsymbol{r_1}, \boldsymbol{r_1}, \omega) W(\boldsymbol{r_2}, \boldsymbol{r_2}, \omega)}} \tag{4}$$

A normalized unit of measure is given by the magnitude of the SDoC for the amount of spatial coherence of a field for two points in space, $\boldsymbol{r_1}$ and $\boldsymbol{r_2}$, and angular frequency ω. Fields at two different points in space are correlated if $|\mu(\boldsymbol{r_1}, \boldsymbol{r_2}, \omega)| = 1$ and are uncorrelated if $|\mu(\boldsymbol{r_1}, \boldsymbol{r_2}, \omega)| = 0$. The field is partially spatially correlated if $0 < |\mu(\boldsymbol{r_1}, \boldsymbol{r_2}, \omega)| < 1$.

2.1.5 Gaussian Schell model source.

The CSD $W(\boldsymbol{\rho_1}, \boldsymbol{\rho_2}, \omega)$ of a GSM source is [2, 14, 22],

$$\begin{aligned} W(\boldsymbol{\rho_1}, \boldsymbol{\rho_2}, \omega) &= \sqrt{S(\boldsymbol{\rho_1}, \omega)}\sqrt{S(\boldsymbol{\rho_2}, \omega)}\mu(|\boldsymbol{\rho_2} - \boldsymbol{\rho_1}|, \omega) \\ S(\boldsymbol{\rho}, \omega) &= A^2 \exp\left(\frac{\rho^2}{2\sigma^2}\right) \\ \mu(\boldsymbol{\rho}, \omega) &= \exp\left(-\frac{|\boldsymbol{\rho}|^2}{2\delta^2}\right) \end{aligned} \tag{5}$$

where A^2, ω, σ, and δ are space independent, but do depend on angular frequency ω, and $\boldsymbol{\rho} = \hat{\boldsymbol{x}}x + \hat{\boldsymbol{y}}y$. When Eq. (5) is substituted into Eq. (4), the magnitude of the SDoC becomes [2, 9],

$$|\mu(\boldsymbol{\rho_2} - \boldsymbol{\rho_1}, \omega)| = \exp\left(-\frac{|\boldsymbol{\rho_2} - \boldsymbol{\rho_1}|^2}{2\delta_{\alpha\beta}^2}\right) \tag{6}$$

and is only dependent on the separation distance of $\boldsymbol{\rho_2} - \boldsymbol{\rho_1}$. The source coherence length δ is the distance between the two points $|\boldsymbol{\rho_2} - \boldsymbol{\rho_1}|$ where the magnitude of the SDoC in Eq. (6) falls off by $1/e^2$ of its original on-axis value. If the GSM source is spatially coherent and the two points are correlated if $|\boldsymbol{\rho_2} - \boldsymbol{\rho_1}| \ll \delta$; else the GSM is spatially incoherent and the two points are uncorrelated if $|\boldsymbol{\rho_2} - \boldsymbol{\rho_1}| \gg \delta$. The GSM source is partially spatially coherent if $0 < |\boldsymbol{\rho_2} - \boldsymbol{\rho_1}| < \delta$.

2.1.6 Cross-spectral density matrix.

The cross-spectral density matrix CSDM $\mathbf{W}(\boldsymbol{\rho_1}, \boldsymbol{\rho_2}, \omega)$ is used to analyze the spatial coherence of vector fields in the space frequency domain [7, 22]. The CSDM is the outer product generated from electric field vectors,

$$\begin{aligned} E(\boldsymbol{\rho}, \omega) &= E_x(\boldsymbol{\rho}, \omega)\hat{\boldsymbol{x}} + E_y(\boldsymbol{\rho}, \omega)\hat{\boldsymbol{y}} \\ &= \begin{bmatrix} E_x(\boldsymbol{\rho}, \omega) \\ E_y(\boldsymbol{\rho}, \omega) \end{bmatrix} \end{aligned} \tag{7}$$

such that

$$\begin{aligned} \mathbf{W}(\boldsymbol{\rho_1}, \boldsymbol{\rho_2}; \omega) &= \left\langle E(\boldsymbol{\rho_1}, \omega) E^H(\boldsymbol{\rho_2}, \omega) \right\rangle \\ &= \left\langle \begin{bmatrix} E_x(\boldsymbol{\rho_1}, \omega) \\ E_y(\boldsymbol{\rho_2}, \omega) \end{bmatrix} \begin{bmatrix} E_x^*(\boldsymbol{\rho_1}, \omega) & E_y^*(\boldsymbol{\rho_2}, \omega) \end{bmatrix} \right\rangle \\ &= \left\langle \begin{bmatrix} E_{x1} \\ E_{y1} \end{bmatrix} \begin{bmatrix} E_{x2}^* & E_{y2}^* \end{bmatrix} \right\rangle \\ &= \begin{bmatrix} \langle E_{x1} E_{x2}^* \rangle & \langle E_{x1} E_{y2}^* \rangle \\ \langle E_{y1} E_{x2}^* \rangle & \langle E_{y1} E_{y2}^* \rangle \end{bmatrix} \end{aligned} \tag{8}$$

and

$$W(\boldsymbol{\rho_1}, \boldsymbol{\rho_2}; \omega) = \left\langle E_\alpha(\boldsymbol{\rho_1}, \omega) E_\beta^*(\boldsymbol{\rho_2}, \omega) \right\rangle, \quad \begin{pmatrix} \alpha = x, y \\ \beta = x, y \end{pmatrix} \tag{9}$$

where ^{H} denotes the conjugate transpose and $E_x(\boldsymbol{\rho}, \omega)$ and $E_y(\boldsymbol{\rho}, \omega)$ are two mutually orthogonal field components perpendicular to the direction of propagation.

2.2. Polarization

Given the CSDM in Eq. (8), the degree of polarization (DoP) gives a space and angular frequency dependent relationship for how much of the light is polarized [14, 22]:

$$P(\boldsymbol{\rho},\omega) = \sqrt{1 - \frac{4\mathrm{Det}\left\{W(\boldsymbol{\rho},\boldsymbol{\rho},\omega)\right\}}{\mathrm{Tr}\left\{W(\boldsymbol{\rho},\boldsymbol{\rho},\omega)\right\}}} \tag{10}$$

where $\mathrm{Det}\{...\}$ is the determinant and $\mathrm{Tr}\{...\}$ is the trace of the CSDM. The field is polarized if $P(\boldsymbol{\rho},\omega) = 1$, is unpolarized if $P(\boldsymbol{\rho},\omega) = 0$, and is partially polarized when $0 < P(\boldsymbol{\rho},\omega) < 1$. Another way of finding polarization is to use Stokes vectors where the components of the vector are [18]

$$\begin{aligned} S_0(\boldsymbol{\rho},\omega) &= W_{xx}(\boldsymbol{\rho},\boldsymbol{\rho},\omega) + W_{yy}(\boldsymbol{\rho},\boldsymbol{\rho},\omega) \\ S_1(\boldsymbol{\rho},\omega) &= W_{xx}(\boldsymbol{\rho},\boldsymbol{\rho},\omega) - W_{yy}(\boldsymbol{\rho},\boldsymbol{\rho},\omega) \\ S_2(\boldsymbol{\rho},\omega) &= W_{xy}(\boldsymbol{\rho},\boldsymbol{\rho},\omega) + W_{yx}(\boldsymbol{\rho},\boldsymbol{\rho},\omega) \\ S_3(\boldsymbol{\rho},\omega) &= j[W_{yx}(\boldsymbol{\rho},\boldsymbol{\rho},\omega) - W_{xy}(\boldsymbol{\rho},\boldsymbol{\rho},\omega)] \end{aligned} \tag{11}$$

By transforming the Stokes vectors to spherical coordinates and normalizing to S_0 the following relationships are formed [4]:

$$\begin{aligned} S_0(\boldsymbol{\rho},\omega) &= 1 \\ S_1(\boldsymbol{\rho},\omega) &= S_0\cos(2\chi)\cos(2\Psi) \\ S_2(\boldsymbol{\rho},\omega) &= S_0\cos(2\chi)\sin(2\Psi) \\ S_3(\boldsymbol{\rho},\omega) &= S_0\sin(2\chi) \end{aligned} \tag{12}$$

$$
\begin{aligned}
P(\boldsymbol{\rho},\omega) &= \frac{\sqrt{S_1^2(\boldsymbol{\rho},\omega)+S_2^2(\boldsymbol{\rho},\omega)+S_3^2(\boldsymbol{\rho},\omega))}}{S_0(\boldsymbol{\rho},\omega)} \\
\Psi &= \frac{1}{2}\arctan\left(\frac{S_2(\boldsymbol{\rho},\omega)}{S_0(\boldsymbol{\rho},\omega)}\right) \\
\chi &= \frac{1}{2}\arcsin\left(\frac{S_3(\boldsymbol{\rho},\omega)}{S_0(\boldsymbol{\rho},\omega)}\right)
\end{aligned}
\tag{13}
$$

P is the DoP, Ψ is the angle of polarization (AoP) measured from the x-axis, and χ is ellipticity. The factor of two before Ψ in Eq. (12) represents the fact that any polarization ellipse is indistinguishable from one rotated by 180°.

III. Methodology

The experimental set-up utilizes much of the same configuration as described in Ref. [9] with some significant differences. The configuration is constructed on a pneumatically dampened table with black out curtains to reduce vibration and eliminate ambient light from contaminating the results. Since an objective of the research is to reduce the optical train footprint and mitigate registration errors, this new configuration has consolidated and/or eliminated five optical elements that were present in previous research to include a Gaussian amplitude filter, two 4-f systems, and a variable retarder. The experiment begins with an ESGM source produced by a HeNe gas laser whose radiation is almost completely coherent and completely polarized with a wavelength of $\lambda = 632.8$nm. Referring to Fig. 1, the beam from the source passes through a beam expander (BE). The BE is adjusted to fill a minimum region of interest while maintaining collimation. A half-wave plate (HWP) and linear polarizer (LP) follow after the BE. The purpose of these two elements is to control the relative amplitude of the beam and isolate the two desired polarization states E_x and E_y by aligning the HWP to 45°. For notation, the open circles refer to vertical polarization and the double headed arrow refers to horizontal polarization.

A polarized beam splitter (PBS) follows the LP and HWP and passes only the horizontally polarized light while reflecting the vertically polarized light. The resulting two paths are the vertical path labeled as Path 1 and the horizontal leg labeled as Path 2.

The SLM is manufactured to respond to only vertically polarized light. As such, after reflecting off of Mirror 1 at the beginning of Path 1, a HWP and LP are used to convert horizontally polarized light from the exiting beam of the PBS1 into vertically polarized light. This will ensure that only vertically polarized light is incident on the SLMs. The LP following the HWP plate also helps correct for any polarization errors

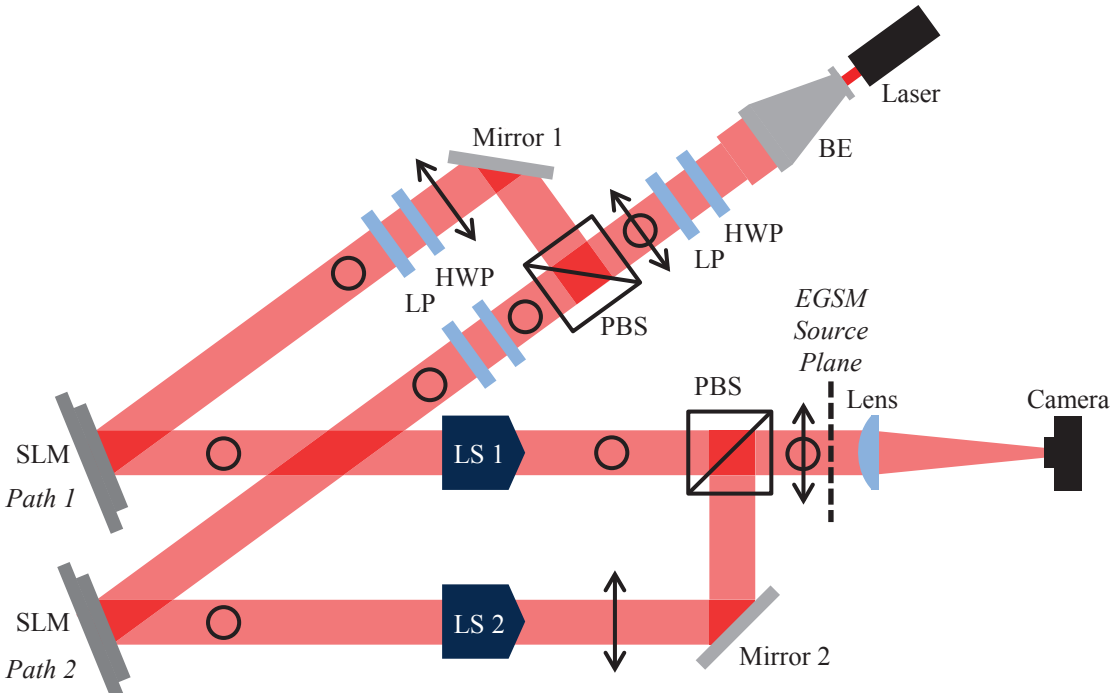

Figure 1. Experimental set-up showing a simplified model of the bench set-up. The setup consist of two sub blocks: LS1 and LS2.

that were introduced after exiting the HWP and prior to being incident on the SLM.

Referring to Fig. 2 and looking at Path 1, immediately after the SLM there is a 4-f lens system (LS). LS1 consists of an iris in the focal plane located between the two plano-convex lens with focal lengths of 350 mm. The iris as depicted in Fig. 3(b) is adjusted visually and removes unwanted diffraction orders allowing only the first order to propagate forward. Allowing additional orders through would contaminate the resulting EGSM. In addition, LS1 translates the SLM plane along the table to prevent additional phase curvature prior to entering the PBS2 as well as maintaining a common path length with Path 2. After the iris is a HWP and LP. The primary function of the HWP in Path 1 is to help control relative power. The LP is used to help clean and isolate the now vertical polarization state after exiting the HWP.

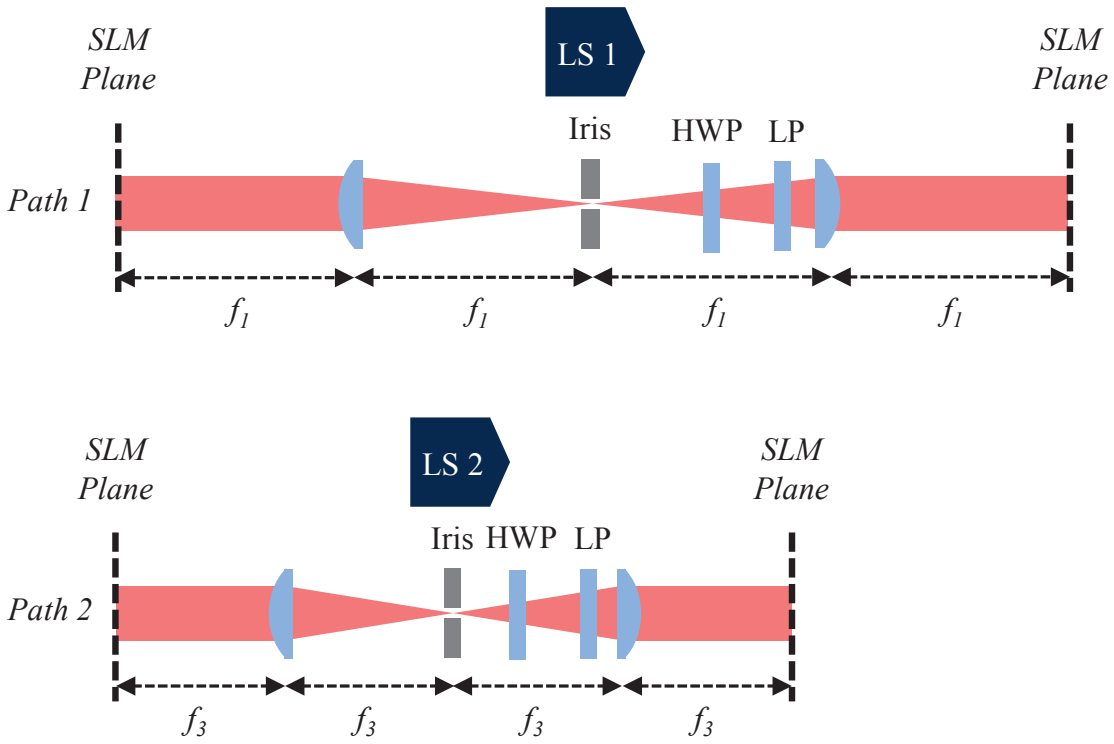

Figure 2. Optical elements in Path 1 and Path 2. Path 1 is the horizontal polarized leg and Path 2 is the vertically polarized leg.

Referring to Fig. 2 and looking at Path 2; immediately after the SLM, there is a 4-f LS. LS2 consists of an iris in the focal plane located between two plano-convex lenses with focal lengths of 375 mm. The iris was adjusted visually and removes unwanted diffraction orders allowing only the first order to propagate forward. Allowing additional orders through would contaminate the resulting EGSM. In addition, LS2 translates the SLM plane to prevent additional phase curvature prior to entering the PBS2 as well as maintaining a common path length with Path 1. After the iris is a HWP and LP. The primary function of the HWP plate in Path 2 is to rotate the vertically polarized light back to horizontally polarized light prior to entering PBS2. The HWP is also used to control relative power and the LP is used to help clean and isolate the now horizontal polarization state. Mirror 2 is used to spatially offset Path 2 from Path 1 so both paths are focused at opposite corners of the camera. This can be done for this experiment since only S_0 and S_1 are calculated.

Immediately following the PBS2, the now recombined partially polarized light enters a lens with focal length of 1500 mm. This lens translates the propagated polarized light into the far field where the resulting irradiance is measured.

3.1. Polarization analyzer

To collect the desired data from the generated EGSM source, a Lumenera LU135R camera with 1392 $\times$ 1024 pixels with 4.65 μm pitch is positioned at the focal plane of the 1500 mm lens as seen in Fig. 1. Since S_0 and S_1 are the two Stokes parameters of interest, only 0° and 90° states need to be measured. To ensure that the two separate measurements are of the same instance, both E_x and E_y are spatially offset on the camera detector using Mirror 2. This is easily done as both legs of the EGSM source in Fig. 2 are already separated and steerable for alignment, and the detector is large enough to accommodate both irradiance patterns. E_x and E_y are both steered to

opposite corners of the camera resulting in a subdivided detector space of 520×696 pixels.

3.2. EGSM source and building correlated phase screens

An EGSM is a vector form of a traditional GSM [16]. The following section will outline how to build an EGSM source with correlation between the two orthogonal field components using the CSDM and correlated phase screens. The following calculations can be found in Ref. [2, 9], but are reproduced here for completeness.

3.2.1 Gaussian Schell-model source simulation.

In the source plane of a field centered at the origin $z = 0$ the CSD using Eq. (8) is

$$W(\boldsymbol{\rho_1'}, \boldsymbol{\rho_2'}; \omega) = \left\langle E(\boldsymbol{\rho_1'}, \omega) E^*(\boldsymbol{\rho_2'}, \omega) \right\rangle \tag{14}$$

where $\boldsymbol{\rho'} = \hat{\boldsymbol{x}}x + \hat{\boldsymbol{y}}y$ and W is dependent on angular frequency ω. The cross-spectral density of a GSM model source can be characterized using Eq. (14) [2, 22]

$$\begin{aligned} W_{\alpha\beta}(\boldsymbol{\rho_1'}, \boldsymbol{\rho_2'}, 0; \omega) &= \sqrt{S_\alpha(\boldsymbol{\rho_1'}; \omega)} \sqrt{S_\beta(\boldsymbol{\rho_2'}; \omega)} \mu_{\alpha\beta} \left(\left| \boldsymbol{\rho_1'} - \boldsymbol{\rho_2'} \right| ; \omega \right) \\ S_\alpha(\boldsymbol{\rho'}, \omega) &= A_\alpha^2 \exp\left(\frac{-\rho^{2'}}{2\sigma_\alpha^2} \right) \\ \mu_{\alpha\beta}(\left| \boldsymbol{\rho_1'} - \boldsymbol{\rho_2'}; \omega \right|) &= B_{\alpha\beta} \exp\left(\frac{-\left| \boldsymbol{\rho_1'} - \boldsymbol{\rho_2'} \right|^2}{2\delta_{\alpha\beta}^2} \right) \end{aligned} \tag{15}$$

where $\alpha, \beta = x, y$, S_α is the spectral density, and $\mu_{\alpha\beta}$ is the spectral correlation function. In addition, σ_α and $\delta_{\alpha\beta}$ are the r.m.s. widths of the spectral density and correlation profiles. The field components E_x and E_y in the source plane can be

defined as

$$\begin{aligned} E(\boldsymbol{\rho'},\mathbf{0}) &= \hat{x}E_x(\boldsymbol{\rho'}) + \hat{y}E_y(\boldsymbol{\rho'}) \\ E_\alpha(\boldsymbol{\rho'}) &= C_\alpha \exp\left(\frac{-\rho^{2'}}{4\sigma_\alpha^2}\right) \exp\left[\mathrm{j}\phi_\alpha(\boldsymbol{\rho'})\right] \end{aligned} \tag{16}$$

where $C_\alpha = |C_\alpha| \exp(\mathrm{j}\theta_\alpha)$ is a complex constant and $\phi_\alpha(\boldsymbol{\rho'})$ is the random phase contribution due to the screen. Performing the autocorrelation to populate the CSDM yields,

$$\begin{aligned} \left\langle E(\boldsymbol{\rho'_1},0), E^*(\boldsymbol{\rho'_2},0)\right\rangle &= \begin{bmatrix} \left\langle E_x(\boldsymbol{\rho'_1},0), E_x^*(\boldsymbol{\rho'_2},0)\right\rangle & \left\langle E_x(\boldsymbol{\rho'_1},0), E_y^*(\boldsymbol{\rho'_2},0)\right\rangle \\ \left\langle E_y(\boldsymbol{\rho'_1},0), E_x^*(\boldsymbol{\rho'_2},0)\right\rangle & \left\langle E_y(\boldsymbol{\rho'_1},0), E_y^*(\boldsymbol{\rho'_2},0)\right\rangle \end{bmatrix} \\ \left\langle E_\alpha(\boldsymbol{\rho'_1},0), E_\beta^*(\boldsymbol{\rho_2},0)\right\rangle &= C_\alpha C_\beta^* \exp\left[-\left(\frac{\rho_1^{2'}}{4\sigma_\alpha^2}\right) + \left(\frac{\rho_2^{2'}}{4\sigma_\beta^2}\right)\right] \left\langle \exp[\mathrm{j}\phi_\alpha(\boldsymbol{\rho'_1})] \exp[-\mathrm{j}\phi_\beta(\boldsymbol{\rho'_2})]\right\rangle \end{aligned} \tag{17}$$

3.2.2 Phase screen parameters.

In Eq. (17), the expectation $\left\langle \exp[\mathrm{j}\phi_\alpha(\boldsymbol{\rho'_1})] \exp[-\mathrm{j}\phi_\beta(\boldsymbol{\rho'_2})]\right\rangle$ is recognized to be the joint characteristic function (JCF) of a Gaussian random process where ϕ_α and ϕ_β are evaluated at $\omega_1 = 1$ and $\omega_2 = -1$, respectively [6]. The phase screen realizations are sample functions drawn from two correlated Gaussian random processes. If the Gaussian random processes are not correlated, then the two phase screens will be independent. The expectation can be written as [2, 6, 9],

$$\begin{aligned} \left\langle \exp[\mathrm{j}\phi_\alpha(\boldsymbol{\rho'_1})] \exp[\mathrm{j}\phi_\beta(\boldsymbol{\rho'_2})]\right\rangle = \exp\Bigg\{ &-\frac{1}{2}\left(\sigma_{\phi_\alpha}^2 + \sigma_{\phi_\beta}^2\right) \\ &\left[1 - \frac{2\sigma_{\phi_\alpha}\sigma_{\phi_\beta}}{\sigma_{\phi_\alpha}^2 + \sigma_{\phi_\beta}^2} \rho_{\phi_\alpha\phi_\beta} \gamma_{\phi_\alpha\phi_\beta}\left(|\boldsymbol{\rho_1} - \boldsymbol{\rho_2}|\,; l_{\phi_\alpha\phi_\beta}\right)\right]\Bigg\} \end{aligned} \tag{18}$$

where σ_{ϕ_α} and σ_{ϕ_β} are the standard deviations of the phase screens ϕ_α and ϕ_β, respectively; $\rho_{\phi_\alpha\phi_\beta}$ is the correlation coefficient of the phase screens (not to be confused with μ) bounded by $0 \leq \rho_{\phi_\alpha\phi_\beta} \leq 1$; and $\gamma_{\phi_\alpha\phi_\beta}$ is the normalized cross-correlation

function taken to be Gaussian-shaped,

$$\gamma_{\phi_\alpha\phi_\beta}\left(\left|\boldsymbol{\rho_1'}-\boldsymbol{\rho_2'}\right|^2\right)=\exp\left(-\frac{\left|\boldsymbol{\rho_1'}-\boldsymbol{\rho_2'}\right|^2}{l^2_{\phi_\alpha\phi_\beta}}\right) \tag{19}$$

Here, $l_{\phi_\alpha\phi_\beta}$ is the spatial cross-correlation radius of the phase screens ϕ_α and ϕ_β. Assuming that $\frac{\left(\sigma^2_{\phi_\alpha}+\sigma^2_{\phi_\beta}\right)}{2}\gg 1$, then $\gamma_{\phi_\alpha\phi_\beta}\approx 1-\left|\boldsymbol{\rho_1'}-\boldsymbol{\rho_2'}\right|^2/l^2_{\phi_\alpha\phi_\beta}$. Substituting the approximation into Eq. (18) and then into Eq. (17) and simplifying yields,

$$\begin{aligned}\left\langle E_\alpha(\boldsymbol{\rho_1'})E_\beta(\boldsymbol{\rho_2'})\right\rangle = C_\alpha C_\beta^2\exp\left[-\left(\frac{\boldsymbol{\rho_1^{2'}}}{4\sigma_\alpha^2}+\frac{\boldsymbol{\rho_2^{2'}}}{4\sigma_\beta^2}\right)\right]\exp\left[-\frac{1}{2}\left(\sigma^2_{\phi_\alpha}-2\rho_{\phi_\alpha\phi_\beta}\sigma_{\phi_\alpha}\sigma_{\phi_\beta}+\sigma^2_{\phi_\beta}\right)\right]\\ \exp\left[-\frac{\left|\boldsymbol{\rho_1'}-\boldsymbol{\rho_2'}\right|^2}{l^2_{\phi_\alpha\phi_\beta}/\sigma_{\phi_\alpha}\sigma_{\phi_\beta}\rho_{\phi_\alpha\phi_\beta}}\right]\end{aligned} \tag{20}$$

Comparing Eq. (15) to Eq. (20) produces the following relationships of beam parameters on the left of the equal sign to phase screen parameters to the right of the equal sign:

$$\begin{aligned}\delta_{xx}&=\frac{1}{\sqrt{2}}\frac{l_{\phi_{xx}}}{\sigma_{\phi_x}}\\ \delta_{yy}&=\frac{1}{\sqrt{2}}\frac{l_{\phi_{yy}}}{\sigma_{\phi_y}}\\ \delta_{xy}&=\frac{1}{\sqrt{2}}\frac{l_{\phi_{xy}}}{\sqrt{\sigma_{\phi_x}\sigma_{\phi_y}\rho_{\phi_x\phi_y}}}\\ |B_{xy}|&=\exp\left[-\frac{1}{2}\left(\sigma^2_{\phi_x}-2\rho_{\phi_x\phi_y}\sigma_{\phi_x}\sigma_{\phi_y}+\sigma^2_{\phi_y}\right)\right]\end{aligned} \tag{21}$$

Of note, if the fields of E_x and E_y are uncorrelated, $B_{xy}=0$.

3.2.3 Generating phase screens.

Let ϕ and $\tilde{\phi}$ be Fourier transform pairs such that [2, 23]

$$\begin{aligned}\tilde{\phi}(f_x, f_y) &= \iint_{-\infty}^{\infty} \phi(x,y) \exp(-\mathrm{j}2\pi f_x x) \exp(-\mathrm{j}2\pi f_y y) dx dy \\ \phi(x,y) &= \iint_{-\infty}^{\infty} \tilde{\phi}(f_x, f_y) \exp(\mathrm{j}2\pi f_x x) \exp(\mathrm{j}2\pi f_y y) df_x df_y\end{aligned} \tag{22}$$

Since ϕ_α obeys Gaussian statistics,

$$\begin{aligned}\langle \phi_x(x,y) \rangle = \langle \phi_y(x,y) \rangle = \langle \phi_\alpha(x,y) \rangle = 0 \\ \langle \phi_\alpha(x_1,y_1) \phi_\alpha^*(x_2,y_2) \rangle = \sigma_{\phi_\alpha}^2 \exp\left(-\frac{\left| \boldsymbol{\rho_1'} - \boldsymbol{\rho_2'} \right|^2}{l_{\phi_\alpha \phi_\alpha}^2} \right)\end{aligned} \tag{23}$$

Expanding Eq. (23) in a Fourier series gives

$$\begin{aligned}\phi_\alpha(x,y) &= \mathrm{Re}\left[\sum_{m,n} \varphi_{\alpha m,n} \exp\left(\mathrm{j}2\pi \frac{m}{L} x \right) \exp\left(\mathrm{j}2\pi \frac{n}{L} y \right) \right] \\ &= \sum_{mn} \varphi_{\alpha mn}^r \cos\left[\frac{2\pi}{L} (mx + ny) \right] - \sum_{mn} \varphi_{\alpha mn}^i \sin\left[\frac{2\pi}{L} (mx + ny) \right]\end{aligned} \tag{24}$$

where $\varphi_{\alpha mn}$ are Fourier coefficients, φ^r and φ^i are the real and imaginary parts of φ, and $L = \Delta N$ is the size of the discrete gird. Taking the autocorrelation of Eq. (24) and retaining only the real part gives [2]

$$\langle \phi_\alpha(x_1,y_1) \phi_\alpha^*(x_2,y_2) \rangle = \sum_{m,n} \sum_{p,q} \left\langle \varphi_{\alpha mn}^r \varphi_{\alpha pq}^r \right\rangle cos\left[\frac{2\pi}{L} (mx_1 + ny_1 - px_2 - qy_2) \right] \tag{25}$$

Equation (25) must be equal to the autocorrelation using Eq. (22) such that

$$\begin{aligned}\langle \phi_\alpha(x_1,y_1)\phi_\alpha^*(x_2,y_2)\rangle = \iint_{-\infty}^{\infty} \Phi_{\phi_\alpha\phi_\alpha}(f_x,f_y)\exp\left[\mathrm{j}2\pi f_x(x_1-x_2)\right] \\ \exp\left[\mathrm{j}2\pi f_y(y_1-y_2)\right] df_x df_y \\ \Phi_{\phi_\alpha\phi_\alpha} = \sigma_{\phi_\alpha}^2 \pi l_{\phi_\alpha\phi_\alpha}^2 \exp\left[-\pi^2 l_{\phi_\alpha\phi_\alpha}^2\left(f_x^2+f_y^2\right)\right]\end{aligned} \tag{26}$$

where $\Phi_{\phi_\alpha\phi_\alpha}$ is the power spectral density. Since $\Phi_{\phi_\alpha\phi_\alpha}$ is real and even, the integrals in Eq. (26) can be expressed as the following Rieman sums,

$$\langle \phi_\alpha(x_1,y_1)\phi_\alpha^*(x_2,y_2)\rangle = \sum_{m,n} \Phi_{\phi_\alpha\phi_\alpha}\left(\frac{m}{L}\frac{n}{L}\right)\cos\left\{\frac{2\pi}{L}\left[m(x_1-x_2)+n(y_1-y_2)\right]\right\}\frac{1}{L}\frac{1}{L}. \tag{27}$$

By comparing Eq. (27) to Eq. (25), i.e., setting $m=p$ and $n=q$, the following relationship is made:

$$\begin{aligned}\left\langle \varphi_{\alpha mn}^r \varphi_{\alpha pq}^r \right\rangle = \left\langle \varphi_{\alpha mn}^i \varphi_{\alpha pq}^i \right\rangle = \Phi_{\phi_\alpha\phi_\alpha}\left(\frac{m}{L},\frac{n}{L}\right)\delta_{mp}\delta_{nq}\frac{1}{L^2} \\ \left\langle (\varphi^r)^2 \right\rangle = \Phi_{\phi_\alpha\phi_\alpha}\left(\frac{m}{L},\frac{n}{L}\right)\frac{1}{L^2}.\end{aligned} \tag{28}$$

Here, δ_{mp} and δ_{nq} are Kronekcer deltas. Equation (28) is further simplified by Eq. (24)

$$\begin{aligned}\phi_\alpha[i,j] = \mathrm{Re}\Bigg[\sum_{m,n} r_\alpha[m,n]\frac{\sigma_{\phi_\alpha}\sqrt{\pi}l_{\phi_\alpha\phi_\alpha}}{N\Delta}\exp\left\{-\frac{\pi^2 l_{\phi_\alpha\phi_\alpha}^2}{2}\left[\left(\frac{m}{N\Delta}\right)^2+\left(\frac{n}{N\Delta}^2\right)\right]\right\} \\ \exp\left(\mathrm{j}\frac{j2\pi}{N}mi\right)\exp\left(\mathrm{j}\frac{2\pi}{N}nj\right)\Bigg]\end{aligned} \tag{29}$$

3.2.4 Generating correlated phase screens.

To build correlated phase screens, the cross terms of the CSD must be made. Starting with Eq. (29),

$$\begin{aligned}\langle\phi_x[i,j]\phi_y[k,l]\rangle = \sum_{m,n}\sum_{p,q} &\frac{\sigma_{\phi_x}\sqrt{\pi}l_{\phi_x\phi_x}}{N\Delta}\exp\left\{-\frac{\pi^2 l_{\phi_x\phi_x}^2}{2}\left[\left(\frac{m}{N\Delta}\right)^2+\left(\frac{n}{N\Delta}^2\right)\right]\right\}\\ &\frac{\sigma_{\phi_x}\sqrt{\pi}l_{\phi_y\phi_y}}{N\Delta}\exp\left\{-\frac{\pi^2 l_{\phi_y\phi_y}^2}{2}\left[\left(\frac{p}{N\Delta}\right)^2+\left(\frac{q}{N\Delta}^2\right)\right]\right\}\\ &\left\langle\left\{r_x^r[m,n]\cos\left(\frac{2\pi}{N}(mi+nj)\right)-r_x^i[m,n]\sin\left(\frac{2\pi}{N}(mi+nj)\right)\right\}\right.\\ &\left.\left\{r_y^r[p,q]\cos\left(\frac{2\pi}{N}(pk+ql)\right)-r_y^i[p,q]\sin\left(\frac{2\pi}{N}(pk+ql)\right)\right\}\right\rangle\end{aligned} \tag{30}$$

where r^r and r^i are the real and imaginary parts of r, respectively. Expanding lines 3 and 4 of Eq. (30) and reducing leads to

$$\begin{aligned}\left\langle r_x^r[m,n]r_y^r[p,q]\right\rangle &= \left\langle r_x^i[m,n]r_y^i[p,q]\right\rangle = \Gamma\delta_{mp}\delta_{nq}\\ \left\langle r_x^r[m,n]r_y^i[p,q]\right\rangle &= \left\langle r_x^i[m,n]r_y^r[p,q]\right\rangle = 0\end{aligned} \tag{31}$$

where $0 \leqslant \Gamma \leqslant 1$ is a correlation coefficient. Substituting Eq. (30) into Eq. (31) and simplifying gives

$$\begin{aligned}\langle\phi_x[i,j]\phi_y[k,l]\rangle = \sum_{m,n}&\frac{\sigma_{\phi_x}\sigma_{\phi_y}\pi l_{\phi_x\phi_y}\Gamma}{2(\Delta N)^2}\exp\left\{-\pi^2\left(\frac{l_{\phi_x\phi_x}^2+l_{\phi_y\phi_y}^2}{2}\right)\left[\left(\frac{m}{\Delta N}\right)^2+\left(\frac{n}{\Delta N}\right)^2\right]\right\}\\ &\left\{\exp\left(\mathrm{j}\frac{2\pi}{N}m(i-k)\right)\exp\left(\mathrm{j}\frac{2\pi}{N}n(j-l)\right)+\exp\left(\text{-j}\frac{2\pi}{N}m(i-k)\right)\exp\left(\text{-j}\frac{2\pi}{N}n(j-l)\right)\right\}\end{aligned} \tag{32}$$

The complex terms in Eq. (32) are discrete inverse and forward Fourier transform kernels. The function being transformed is even in m and n; therefore, the forward and inverse Fourier transforms yield the same result. Thus, Eq. (32) further reduces

to

$$\langle \phi_x[i,j]\phi_y[k,l]\rangle = \sum_{m,n} \sigma_{\phi_x}\sigma_{\phi_y}\pi\Gamma l_{\phi_x\phi_x} l_{\phi_y\phi_y} \exp\left\{-\pi^2\left(\frac{l^2_{\phi_x\phi_x}+l^2_{\phi_y\phi_y}}{2}\right)\left[\left(\frac{m}{\Delta N}\right)^2+\left(\frac{n}{\Delta N}\right)^2\right]\right\} \exp\left(\mathrm{j}\frac{2\pi}{N}m(i-k)\right)\exp\left(\mathrm{j}\frac{2\pi}{N}n(j-l)\right)\frac{1}{(N\Delta)^2} \tag{33}$$

Comparing the discrete function being transformed in Eq. (33) to the cross-power spectral density function yields the following relations

$$\begin{aligned} l_{\phi_x\phi_y} &= \sqrt{\frac{\Gamma l_{\phi_x\phi_x} l_{\phi_y\phi_y}}{\rho_{\phi_x\phi_y}}} = \sqrt{\frac{l^2_{\phi_x\phi_x}+l^2_{\phi_y\phi_y}}{2}} \\ \Gamma &= \frac{\rho_{\phi_x\phi_y}(l^2_{\phi_x\phi_x}+l^2_{\phi_y\phi_y})}{2l^2_{\phi_x\phi_x}l^2_{\phi_y\phi_y}} \end{aligned} \tag{34}$$

Using Eq. (21) the relationship between source parameters and phase screen design parameters are

$$\begin{aligned} \delta_{xx} &= \frac{l_{\phi_x\phi_x}}{\sqrt{2}\sigma_{\phi_x}} \\ \delta_{yy} &= \frac{l_{\phi_y\phi_y}}{\sqrt{2}\sigma_{\phi_y}} \\ \delta_{xy} &= \frac{l^2_{\phi_x\phi_x}+l^2_{\phi_y\phi_y}}{\sqrt{2}\sqrt{4\Gamma\sigma_{\phi_x}\sigma_{\phi_y}l_{\phi_x\phi_x}l_{\phi_y\phi_y}}} \\ |B_{xy}| &= \exp\left[-\frac{1}{2}\left(\sigma^2_{\phi_x}-\frac{4\Gamma\sigma_{\phi_x}\sigma_{\phi_y}l_{\phi_x\phi_x}l_{\phi_y\phi_y}+\sigma^2_{\phi_y}}{l^2_{\phi_x\phi_x}+l^2_{\phi_y\phi_y}}\right)\right] \end{aligned} \tag{35}$$

3.3. Propagation of CSD

The propagated CSD can be expressed as a Fraunhofer propagation of the form [17, 20]

$$\begin{aligned}\left\langle E_\alpha(\boldsymbol{\rho_1}, f)E^*_\beta(\boldsymbol{\rho_2}, f)\right\rangle = \frac{e^{\mathrm{j}\frac{k}{2f}{\boldsymbol{\rho_1}}^2}}{\text{-j}\lambda f}\frac{e^{-\mathrm{j}\frac{k}{2f}{\boldsymbol{\rho_2}}^2}}{\mathrm{j}\lambda f}\int_{-\infty}^{\infty}\int_{\infty}^{\infty}\left\langle E_\alpha(\boldsymbol{\rho'_1}, 0)E^*_\beta(\boldsymbol{\rho'_2}, 0)\right\rangle \\ \times\, e^{-\mathrm{j}\frac{k}{f}\boldsymbol{\rho_1}\cdot\boldsymbol{\rho'_1}}e^{\mathrm{j}\frac{k}{f}\boldsymbol{\rho_2}\cdot\boldsymbol{\rho'_2}}d^2\boldsymbol{\rho'_1}d^2\boldsymbol{\rho'_2}\end{aligned} \tag{36}$$

where $\boldsymbol{\rho'}$ represents a point in the source plane and $\boldsymbol{\rho}$ is a point in the observation plane. Substituting in the cross spectral density form of the source field from Eq. (5) into E_α and E_β for Eq. (36)

$$\begin{aligned}\left\langle E_\alpha(\boldsymbol{\rho'_1}, f)E^*_\beta(\boldsymbol{\rho'_2}, f)\right\rangle &= \left\langle\sqrt{S_\alpha(\boldsymbol{\rho'_1}, 0)}\sqrt{S_\beta(\boldsymbol{\rho'_2}, 0)}\mu(\boldsymbol{\rho'_1}-\boldsymbol{\rho'_2})\right\rangle, \quad \begin{pmatrix}\alpha = x, y\\ \beta = x, y\end{pmatrix} \\ &= \sqrt{S_\alpha(\boldsymbol{\rho'_1}, 0)}\sqrt{S_\beta(\boldsymbol{\rho'_2}, 0)}\left\langle\mu(\boldsymbol{\rho'_1}-\boldsymbol{\rho'_2})\right\rangle\end{aligned} \tag{37}$$

and isolating the deterministic form while setting z equal to the focal length of the lens f, gives the far field diffraction pattern as

$$\begin{aligned}\left\langle E_\alpha(\boldsymbol{\rho_1}, f)E^*_\beta(\boldsymbol{\rho_2}, f)\right\rangle = \frac{A_\alpha A_\beta}{\lambda^2 f^2}e^{\mathrm{j}\frac{k}{2f}({\boldsymbol{\rho_1}}^2-{\boldsymbol{\rho_2}}^2)}\int_{-\infty}^{\infty}\int_{-\infty}^{\infty}\exp\left(-\frac{{\boldsymbol{\rho'_1}}^2}{4\sigma_\alpha^2}\right)\exp\left(-\frac{{\boldsymbol{\rho'_2}}^2}{4\sigma_\beta^2}\right) \\ \times\exp\left(-\frac{\left|\boldsymbol{\rho'_1}-\boldsymbol{\rho'_2}\right|^2}{2\delta_{\alpha\beta}^2}\right)\exp\left(-\mathrm{j}\frac{k}{f}(\boldsymbol{\rho_1}\cdot\boldsymbol{\rho'_1}-\boldsymbol{\rho_2}\cdot\boldsymbol{\rho'_2})\right)d\boldsymbol{\rho'_1}d\boldsymbol{\rho'_2}\end{aligned} \tag{38}$$

Expanding the term B_{xy}, and regrouping leads to

$$\begin{aligned}\left\langle E_\alpha(\boldsymbol{\rho},f)E^*_\beta(\boldsymbol{\rho},f)\right\rangle =& \frac{A_\alpha A_\beta B_{\alpha\beta}}{\lambda^2 f^2} e^{\mathrm{j}\frac{k}{2f}(\boldsymbol{\rho_1}^2-\boldsymbol{\rho_2}^2)} \int_{-\infty}^{\infty}\int_{-\infty}^{\infty} \exp\left(\frac{-\boldsymbol{\rho_1'}^2}{4\sigma_\alpha^2}\right)\exp\left(\frac{-\boldsymbol{\rho_2'}^2}{4\sigma_\beta^2}\right) \\ &\times \exp\left(\frac{-\boldsymbol{\rho_1'}^2}{2\delta_{\alpha\beta}^2}\right)\exp\left(\frac{-\boldsymbol{\rho_2'}^2}{2\delta_{\alpha\beta}^2}\right)\exp\left(\frac{2\boldsymbol{\rho_1'}\cdot\boldsymbol{\rho_2'}}{2\delta_{\alpha\beta}^2}\right) \\ &\times \exp\Big(-\mathrm{j}\frac{k}{f}(\boldsymbol{\rho_1}\cdot\boldsymbol{\rho_1'}-\boldsymbol{\rho_2}\cdot\boldsymbol{\rho_2'})\Big)d\boldsymbol{\rho_1'}d\boldsymbol{\rho_2'}\end{aligned} \tag{39}$$

Substituting $\boldsymbol{\rho_1'} = x_1' + y_1'$, $\boldsymbol{\rho_2'} = x_2' + y_2'$, $\boldsymbol{\rho_1} = x_1 + y_1$, $\boldsymbol{\rho_2} = x_2 + y_2$, rearranging terms with variable substitutions, allows Eq. (39) to be separable in x_1', x_2', y_1', and y_2':

$$\begin{aligned}\kappa &= \frac{A_x A_y B_{xy}}{\lambda^2 f^2} e^{\mathrm{j}\frac{k}{2f}(\boldsymbol{\rho_1}^2-\boldsymbol{\rho_2}^2)} \\ A &= \frac{1}{4\sigma_x^2} - \frac{1}{2\delta_{xy}^2} \\ B &= \frac{1}{4\sigma_y^2} - \frac{1}{2\delta_{xy}^2} \\ C &= \frac{1}{2\delta_{xy}^2} \\ \left\langle E_\alpha(\boldsymbol{\rho_1},f)E^*_\beta(\boldsymbol{\rho_2},f)\right\rangle &= \kappa\Bigg[\int_{-\infty}^{\infty}\int_{-\infty}^{\infty} e^{-Ax_1^{2'}}e^{-Bx_2^{2'}}e^{-C(x_1'-x_2')^2}e^{\mathrm{j}\frac{k}{f}(x_1'x_1-x_2'x_2)}dx_1'dx_2' \\ &\quad\times\int_{-\infty}^{\infty}\int_{-\infty}^{\infty} e^{-Ay_1^{2'}}e^{-By_2^{2'}}e^{-C(y_1'-y_2')^2}e^{\mathrm{j}\frac{k}{f}(y_1'y_1-y_2'y_2)}dy_1'dy_2'\Bigg] \\ &= \kappa\Bigg[\int_{-\infty}^{\infty} e^{-Ax_1^{2'}}e^{-\mathrm{j}\frac{k}{f}x_1x_1'}\int_{-\infty}^{\infty} e^{-Bx_2'}e^{2Cx_1'x_2'}e^{\mathrm{j}\frac{k}{f}x_2x_2'}dx_2'dx_1'\Bigg] \\ &\quad\times\kappa\Bigg[\int_{-\infty}^{\infty} e^{-Ay_1^{2'}}e^{-\mathrm{j}\frac{k}{f}y_1y_1'}\int_{-\infty}^{\infty} e^{-By_2'}e^{2Cy_1'y_2'}e^{\mathrm{j}\frac{k}{f}y_2y_2'}dy_2'dy_1'\Bigg]\end{aligned} \tag{40}$$

Since the calculations for x_1', x_2' and y_1', y_2' are the same, the following derivations will only focus on x_1', x_2'; the following operations can be repeated by substituting $x_1 = y_1$, and $x_2 = y_2$. Next, completing the square on the cross term $2Cx_1'x_2'$, and substituting

back into Eq. (40) gives

$$\left\langle E_\alpha(\boldsymbol{\rho_1}, f) E^*_\beta(\boldsymbol{\rho_2}, f) \right\rangle = \kappa \left[\int_{-\infty}^{\infty} e^{-Ax_1^{2'}} e^{\frac{C^2}{B}} e^{-\mathrm{j}\frac{k}{f} x_1 x_1'} \int_{-\infty}^{\infty} e^{-B(x_2' - \frac{C}{B}x_1')^2} e^{\mathrm{j}\frac{k}{f} x_2 x_2'} dx_2' dx_1' \right] \tag{41}$$

Letting $T = x_2' - \frac{C}{B}x_1'$ and $x_2' = T + \frac{C}{B}x_1'$, the following integral can be evaluated using the Fourier transform of a shifted Gaussian:

$$\begin{aligned} \left\langle E_\alpha(\boldsymbol{\rho_1}, f) E^*_\beta(\boldsymbol{\rho_2}, f) \right\rangle &= \kappa \left[\int_{-\infty}^{\infty} e^{-Ax_1^{2'}} e^{\frac{C^2}{B} x_1^{2'}} e^{-\mathrm{j}\frac{k}{f} x_1 x_1'} \int_{-\infty}^{\infty} e^{BT^2} e^{\mathrm{j}\frac{k}{f} x_2 (T + \frac{C}{B} x_1')} dT dx_1' \right] \\ &= \kappa \left[\int_{-\infty}^{\infty} e^{-Ax_1^{2'}} e^{\frac{C^2}{B} x_1^{2'}} e^{\mathrm{j}\frac{k}{f} x_2 \frac{C}{B} x_1'} e^{-\mathrm{j}\frac{k}{f} x_1 x_1'} \int_{-\infty}^{\infty} e^{-BT^2} e^{\mathrm{j}\frac{k}{f} x_2 T} dT dx_1' \right] \\ &= \kappa \frac{\sqrt{\pi}}{\sqrt{B}} e^{-\frac{k^2}{4z^2 B} x_2^2} \int_{-\infty}^{\infty} e^{-(A + \frac{C^2}{B}) x_1^{2'}} e^{\mathrm{j}\frac{k}{z} x_1' (x_1 - \frac{C}{B} x_2)} dx_1' \end{aligned} \tag{42}$$

The second integral can be computed the same way using the same shifted Gaussian Fourier transform and setting $\zeta = x_1 - \frac{C}{B}x_2$ and $\eta = A + \frac{C^2}{B}$:

$$\left\langle E_\alpha(\boldsymbol{\rho_1}, f) E^*_\beta(\boldsymbol{\rho_2}, f) \right\rangle = \kappa \left[\frac{\sqrt{\pi}}{\sqrt{B}} e^{-\frac{k^2}{4z^2 B} x_2^2} \frac{\sqrt{\pi}}{\sqrt{\eta}} e^{-\frac{k^2 \zeta^2}{4f^2 \eta}} \right] \tag{43}$$

Finally, expanding the exponential and reducing produces the propagated field in Eq. (44). As mentioned earlier, because the CSD is separable into x and y, the total irradiance can be written as,

$$\begin{aligned} \left\langle E_\alpha(\boldsymbol{\rho_1}, f) E^*_\beta(\boldsymbol{\rho_2}, f) \right\rangle = \kappa \frac{\pi^2}{AB - C^2} &\exp\left[\frac{-k^2}{4f^2} \left(\frac{Ax_2^2 + 2Cx_1x_2 + Bx_1^2}{BA - C^2} \right) \right] \\ &\times \exp\left[\frac{-k^2}{4f^2} \left(\frac{Ay_2^2 + 2Cy_1y_2 + By_1^2}{BA - C^2} \right) \right] \end{aligned} \tag{44}$$

The resulting irradiance is a scaled Gaussian in the focal plane. The widths of the Gaussian diffraction pattern will vary based on spectral density widths σ_x and σ_y and

coherence lengths δ_{xx}, δ_{yy}, and δ_{xy}. Furthermore there is Fourier relationship between spectral density in the source plane and correlation μ in the observation plane. This relationship holds true inversely as well and helps to convey an understanding of the source/observation beam relationship.

3.4. Amplitude control

Amplitude control of an EGSM can be achieved by introducing optical elements into the path of propagation. This is convenient if the desired EGSM source remains fixed. Another way to control amplitude is to use the SLM. Although a SLM by design is manufactured to alter the phase of light, as will be shown, the amplitude can also be controlled. This new contribution and flexibility to the experimental design allows the user to create any beam shape without the need for fixed amplitude optical elements. For example, circular flat-top beams can be made all by controlling the amplitude grating.

3.4.1 SLM discrete grating.

The SLM used is a Boulder NonLinear Systems (BNS) Model P512-0635 XY Series LC SLM with a 512 x 512 pixel array. In order to create a desired gradient along the SLM, a super pixel is created by combining eight individual pixels. This dimension was chosen as it keeps the dimensionality of the SLM square to a 64 x 64 super pixel array, and also allows for better isolation of the first diffraction order as seen in Fig. 3(b) while maintaining high fidelity of the sampled amplitude $|U|$ [11, 12]. This is because as the number of pixels that make a super pixel increase, the diffraction orders move closer together and become more difficult to isolate. Too few pixels will result in under sampling the desired amplitude profile. Figure 3 depicts a grating profile of one super pixel as a function of wavelength λ, where L is the super pixel

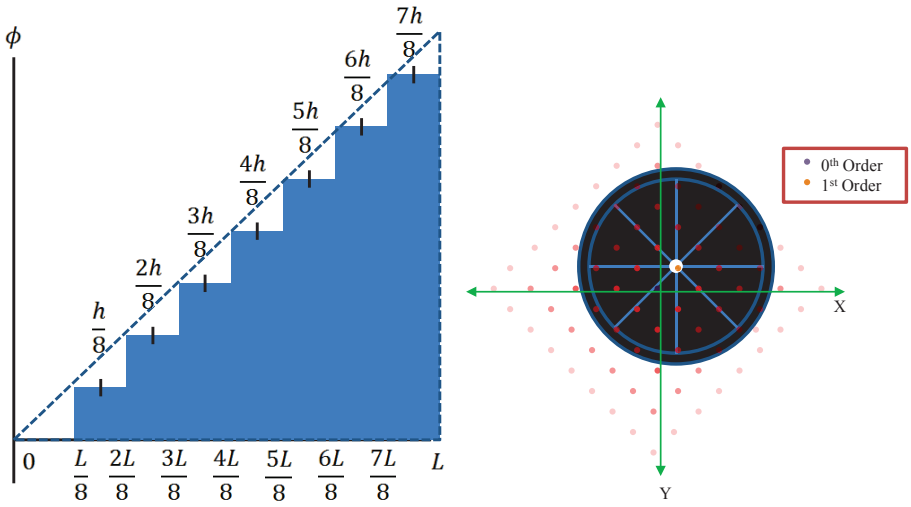

(a) (b)

Figure 3. Subfigure (a) is a model of applying a grating to a SLM super pixel consisting of eight SLM pixels and centered at $(x, y) = 0$. Subfigure (b) shows how a mechanical iris is used to pick out the first order instead of the zeroth order.

length and h is the height of the gradient being applied that will alter the relative phase as can be seen in Fig. 3(a). A grating profile is applied on both SLMs steering the desired E_x and E_y into the first order. Since the theory is the same for both fields due to separability, only E_x will be derived and referenced. The following calculations assume 100% fill factor. In reality, the zeroth order will always have power in it due to the area between pixels that cannot be commanded that gets directed into the zeroth order. Therefore, the first order is used. The transmittance for one super pixel can be expressed as

$$\begin{aligned} T(x) = \Bigg[& \operatorname{rect}\left(\frac{x-\frac{L}{16}}{\frac{L}{8}}\right) + e^{\mathrm{j}\frac{2\pi}{\lambda}\frac{h}{8}} \operatorname{rect}\left(\frac{x-\frac{3L}{16}}{\frac{L}{8}}\right) + e^{\mathrm{j}\frac{2\pi}{\lambda}\frac{2h}{8}} \operatorname{rect}\left(\frac{x-\frac{5L}{16}}{\frac{L}{8}}\right) \\ & + e^{\mathrm{j}\frac{2\pi}{\lambda}\frac{3h}{8}} \operatorname{rect}\left(\frac{x-\frac{7L}{16}}{\frac{L}{8}}\right) + e^{\mathrm{j}\frac{2\pi}{\lambda}\frac{4h}{8}} \operatorname{rect}\left(\frac{x-\frac{9L}{16}}{\frac{L}{8}}\right) + e^{\mathrm{j}\frac{2\pi}{\lambda}\frac{5h}{8}} \operatorname{rect}\left(\frac{x-\frac{11L}{16}}{\frac{L}{8}}\right) \\ & + e^{\mathrm{j}\frac{2\pi}{\lambda}\frac{6h}{8}} \operatorname{rect}\left(\frac{x-\frac{13L}{16}}{\frac{L}{8}}\right) + e^{\mathrm{j}\frac{2\pi}{\lambda}\frac{7h}{8}} \operatorname{rect}\left(\frac{x-\frac{15L}{16}}{\frac{L}{8}}\right) \Bigg] \bigotimes \operatorname{comb}\left(\frac{x}{L}\right) \end{aligned} \tag{45}$$

The expression is convolved with a comb($\frac{x}{L}$) function to represent how the pattern

repeats for a given spatial array length. Taking the Fourier transform of Eq. (45) [5],

$$\begin{aligned}\mathfrak{F}(T) =&\frac{L^2}{8}\text{sinc}\left(\frac{L}{8}f_x\right)\text{comb}(Lf_x)\Bigg[e^{-2\pi\frac{L}{16}f_x}+e^{j\frac{2\pi}{\lambda}\frac{h}{8}}e^{-\text{j}2\pi\frac{3L}{16}f_x}+e^{\text{j}\frac{2\pi}{\lambda}\frac{2h}{8}}e^{-\text{j}2\pi\frac{5L}{16}f_x}\\&+e^{\text{j}\frac{2\pi}{\lambda}\frac{3h}{8}}e^{-\text{j}2\pi\frac{7L}{16}f_x}+e^{\text{j}\frac{2\pi}{\lambda}\frac{5h}{8}}e^{-\text{j}2\pi\frac{7L}{16}f_x}+e^{\text{j}\frac{2\pi}{\lambda}\frac{4h}{8}}e^{-\text{j}2\pi\frac{9L}{16}f_x}\\&+e^{\text{j}\frac{2\pi}{\lambda}\frac{5h}{8}}e^{-\text{j}2\pi\frac{11L}{16}f_x}+e^{\text{j}\frac{2\pi}{\lambda}\frac{6h}{8}}e^{-\text{j}2\pi\frac{13L}{16}f_x}+e^{\text{j}\frac{2\pi}{\lambda}\frac{7h}{8}}e^{-\text{j}2\pi\frac{15L}{16}f_x}\Bigg]\end{aligned}\tag{46}$$

Evaluating Eq. (46) for the first order at $f_x=\frac{1}{L}$ equals

$$\begin{aligned}\mathfrak{F}(T) =&\frac{L^2}{8}\text{sinc}\left(\frac{1}{8}\right)\Bigg[e^{-\text{j}\frac{2\pi}{16}}+e^{\text{j}\frac{2\pi}{\lambda}\frac{h}{8}}e^{-\text{j}2\pi\frac{3}{16}}+e^{\text{j}\frac{2\pi}{\lambda}\frac{2h}{8}}e^{-\text{j}2\pi\frac{5}{16}}\\&+e^{\text{j}\frac{2\pi}{\lambda}\frac{3h}{8}}e^{-\text{j}2\pi\frac{7}{16}}+e^{\text{j}\frac{2\pi}{\lambda}\frac{4h}{8}}e^{-\text{j}2\pi\frac{9}{16}}+e^{\text{j}\frac{2\pi}{\lambda}\frac{5h}{8}}e^{-\text{j}2\pi\frac{11}{16}}\\&+e^{\text{j}\frac{2\pi}{\lambda}\frac{6h}{8}}e^{-\text{j}2\pi\frac{13}{16}}+e^{\text{j}\frac{2\pi}{\lambda}\frac{7h}{8}}e^{-j2\pi\frac{15}{16}}\Bigg]\end{aligned}\tag{47}$$

Equation (47) further reduces using the geometric series identity $a\frac{1-r^n}{1-r}$, multiplying the expression by $-1/-1$, and applying Euler's identity:

$$\begin{aligned}\mathfrak{F}(T) =&\frac{L^2}{8}\text{sinc}\left(\frac{1}{8}\right)e^{-\text{j}\frac{2\pi}{16}}\frac{e^{\text{j}\frac{2\pi}{\lambda}\frac{h}{8}(8)}e^{-\text{j}2\pi\frac{2}{16}(8)}-1}{e^{\text{j}\frac{2\pi}{\lambda}\frac{h}{8}}e^{-\text{j}2\pi\frac{2}{16}}-1}\\=&\frac{L^2}{8}\text{sinc}\left(\frac{1}{8}\right)e^{-\text{j}\frac{2\pi}{16}}\frac{e^{\text{j}\frac{2\pi}{\lambda}h}-1}{e^{\text{j}2\pi[\frac{h}{8\lambda}-\frac{1}{8}]}-1}\\=&\frac{L^2}{8}\text{sinc}\left(\frac{1}{8}\right)e^{-\text{j}\frac{2\pi}{16}}\frac{e^{\text{j}\frac{2\pi}{\lambda}\frac{h}{2}}}{e^{\text{j}\frac{2\pi}{(2)(8)}[\frac{h}{\lambda}-1]}}\frac{e^{\text{j}\frac{2\pi}{\lambda}\frac{h}{2}}-e^{-\text{j}\frac{2\pi}{\lambda}\frac{h}{2}}}{e^{\text{j}\frac{2\pi}{16}(\frac{h}{\lambda}-1)}-e^{-\text{j}\frac{2\pi}{16}(\frac{h}{2}-1)}}\\=&-\frac{L^2}{8}\text{sinc}\left(\frac{1}{8}\right)e^{\text{j}\frac{\pi}{8}}\frac{e^{\text{j}\frac{\pi h}{\lambda}}}{e^{\text{j}\frac{\pi}{8}(\frac{h}{\lambda}-1)}}\frac{\sin\left(\frac{\pi h}{\lambda}\right)}{\sin\left(\frac{\pi}{8}(1-\frac{h}{\lambda})\right)}\\=&\frac{\sin\left[8\frac{\pi}{8}(1-\frac{h}{\lambda})\right]}{\sin\left[\frac{\pi}{8}(1-\frac{h}{\lambda})\right]}\frac{L^2}{8}\text{sinc}\left(\frac{1}{8}\right)e^{-\text{j}\frac{\pi}{8}}\frac{e^{\text{j}\pi(\frac{h}{\lambda}-1)}}{e^{\text{j}\frac{\pi}{8}(\frac{h}{\lambda}-1)}}\end{aligned}\tag{48}$$

Computing the power ratio of the first order using Eq. (48) and applying L'Hospital's

rule and taking the limit as $h \to \lambda$ produces the following power ratio expression for the first order:

$$\frac{|E_x(f_x = \frac{1}{L})|^2}{|E_x(h = \lambda)|^2} = \frac{\sin^2\left[8\frac{\pi}{8}(1 - \frac{h}{\lambda})\right]}{8^2 \sin^2\left[\frac{\pi}{8}(1 - \frac{h}{\lambda})\right]} \tag{49}$$

In general, for steps sizes of N, Eq. (49) can be expressed as

$$\frac{|E_x(f_x = \frac{1}{L})|^2}{|E_x(h = \lambda)|^2} = \frac{\sin^2\left[\pi(1 - \frac{h}{\lambda})\right]}{N^2 \sin^2\left[\frac{\pi}{N}(1 - \frac{h}{\lambda})\right]} \tag{50}$$

Equation (50) is reduced to its final form by approximating the term inside the sine term in the denominator. As N becomes very large, the Taylor series approximation of $\sin(x) = x$, resulting in the denominator reducing to $\pi^2(1 - \frac{h}{\lambda})^2$:

$$\frac{|E_x(f_x = \frac{1}{L})|^2}{|E_x(h = \lambda)|^2} = \text{sinc}^2\left(1 - \frac{h}{\lambda}\right) \tag{51}$$

From here a few important observations can be made. As $h \to \lambda$, all the power goes into the first order. Due to this, commanding off the first order is ideal. Finally, line three of Eq. (49) reduces to a sinc relationship. In the continuous case of a defined grating period, the power in the zeroth order reduces to a similar sinc expression. Thus, the first order achieves adequate sampling with eight pixels and power over the desired range.

Finally, since power is being measured but the field is what is of interest, taking the square root of Eq. (49) produces the final field grating relationship,

$$\frac{E_x(f_x = \frac{1}{L})}{E_x(h = \lambda)} = \text{sinc}\left(1 - \frac{h}{\lambda}\right) \frac{e^{\mathrm{j}\pi(\frac{h}{\lambda} - 1)}}{e^{\mathrm{j}\frac{\pi}{8}(\frac{h}{\lambda} - 1)}} \tag{52}$$

This expression controls the amplitude of the EGSM while also steering the field into the first order where it can be observed in the far field [12].

3.5. Calculating experimental Stokes parameters, DoP, and SDoC

The experimental set-up by its nature measures S_0 directly with one camera. Thus, S_0 and S_1 can be calculated from the measured irradiances from their definition in Eq. 11. The DoP can also be calculated directly using Eq. (13). Since the polarimeter only measures S_0 and S_1, S_2 and S_3 are not calculated and will not be addressed from here on.

The last desired measurement is the SDoC. This is not directly measurable nor able to be calculated using the gathered irradiance images because an electric field would have to be captured by the detector. Given the DoC of each CSDM element as defined by

$$\mu_{\alpha\beta} = \frac{W_{\alpha\beta}(\boldsymbol{\rho_1}, \boldsymbol{\rho_2})}{\sqrt{W_{\alpha\beta}(\boldsymbol{\rho_1}, \boldsymbol{\rho_1}) W_{\alpha\beta}(\boldsymbol{\rho_2}, \boldsymbol{\rho_2})}}, \quad \begin{pmatrix} \alpha = x, y \\ \beta = x, y \end{pmatrix} \tag{53}$$

A comparable measurement needs to be taken to obtain this quantity. This can be done by taking the modulus squared of Eq. (53):

$$|\mu_{\alpha\beta}|^2 = \frac{W_{\alpha\beta}(\boldsymbol{\rho_1}, \boldsymbol{\rho_2}) W^*_{\alpha\beta}(\boldsymbol{\rho_1}, \boldsymbol{\rho_2})}{S_\alpha(\boldsymbol{\rho_1}) S_\beta(\boldsymbol{\rho_2})}, \quad \begin{pmatrix} \alpha = x, y \\ \beta = x, y \end{pmatrix} \tag{54}$$

Applying the Gaussian Moment Theorem for the measured intensities in Line 1 of

Eq. (55) gives Line 2 and Line 3 as

$$\begin{aligned}\langle I_\alpha(\boldsymbol{\rho_1})I_\beta(\boldsymbol{\rho_2})\rangle &= \langle E^*_\alpha(\boldsymbol{\rho_1})E^*_\beta(\boldsymbol{\rho_2})E_\alpha(\boldsymbol{\rho_1})E_\beta(\boldsymbol{\rho_2})\rangle \\ &= \langle E^*_\alpha(\boldsymbol{\rho_1})E_\alpha(\boldsymbol{\rho_1})\rangle\langle E^*_\beta(\boldsymbol{\rho_2})E_\beta(\boldsymbol{\rho_2})\rangle + \langle E^*_\alpha(\boldsymbol{\rho_1})E_\beta(\boldsymbol{\rho_2})\rangle\langle E^*_\beta(\boldsymbol{\rho_2})E_\alpha(\boldsymbol{\rho_1})\rangle \\ &= S_\alpha(\boldsymbol{\rho_1})S_\beta(\boldsymbol{\rho_2}) + W_{\alpha\beta}(\boldsymbol{\rho_1},\boldsymbol{\rho_2})W^*_{\alpha\beta}(\boldsymbol{\rho_1},\boldsymbol{\rho_2}), \quad (\alpha = x,y \text{ and } \beta = x,y)\end{aligned} \tag{55}$$

This expression simplifies to

$$|\mu_{\alpha\beta}|^2 = \frac{\langle I_\alpha(\boldsymbol{\rho_1})I_\beta(\boldsymbol{\rho_2})\rangle}{S_\alpha(\boldsymbol{\rho_1})S_\beta(\boldsymbol{\rho_2})} - 1, \quad \begin{pmatrix}\alpha = x,y \\ \beta = x,y\end{pmatrix} \tag{56}$$

which is the normalized fourth-order correlation function (FOCF) expanded in terms of the DoC [3, 21]. In order to provide cleaner results when comparing the gathered experimental data to the simulated and theoretical data, the relationship is rearranged such that,

$$\langle I_\alpha(\boldsymbol{\rho_1})I_\beta(\boldsymbol{\rho_2})\rangle = W_{\alpha\beta}(\boldsymbol{\rho_1},\boldsymbol{\rho_2})W^*_{\alpha\beta}(\boldsymbol{\rho_1},\boldsymbol{\rho_2}) + S_\alpha(\boldsymbol{\rho_1})S_\beta(\boldsymbol{\rho_2}), \quad \begin{pmatrix}\alpha = x,y \\ \beta = x,y\end{pmatrix} \tag{57}$$

The right-hand side of Eq. (57) is computed from the theoretical expression given in Eq. (44).

IV. Analysis and Results

Chapter 4 presents the results of two different EGSM sources generated using the SLM amplitude grating approach. Source beam parameters for both cases are identified in Table 1. The design of Experiment I creates a linear partially polarized beam with polarization changes across its profile in the observation plane with particular emphasis on S_1. Experiment II also creates a linear partially polarized beam in the observation plane, but is generated from an unpolarized source. The intent of both these experiments is to demonstrate a level of control seen in Ref. [9], but showcase a degree of freedom in design with the use of amplitude control via the SLM while reducing registration errors observed in previous research results

Table 1. EGSM Source Parameters

	Exp. I		Exp. II		Ref. [9]	
Parameter	Desired	Actual	Desired	Actual	Desired	Actual
A_x	1	1	1.3	1.3	1.3	1.3
A_y	1.5	1.5	1.3	1.3	1	1
$\angle B_{xy}$	0	0	0	0	0	0
σ_x (mm)	1	1	.4286	.4286	2.8	2.8
σ_y (mm)	1	1	.4286	.4286	2.1	2.1
δ_{xx} (mm)	.5	.5	.16	.16	.40406	.40406
δ_{yy} (mm)	.22	.22	.5	.5	.30305	.30305
δ_{xy} (mm)	.45	.22	.9	0	.44447	.44447
$\lvert B_{xy} \rvert$	0	0	0	0	0	2.5513e-6

Results for Experiment I and II are plotted from raw measurements that have been centered and radially averaged to compensate for drift over the ensemble collection.

Table 2. Phase Screen Parameters

Parameter	Exp. I	Exp. II	Ref. [9]
$l_{\phi_x\phi_x}$ (mm)	.22	.7109	2.9
$l_{\phi_y\phi_y}$ (mm)	.97	2.2	1.7
σ_{ϕ_x}	3.1416	3.1416	5.0552
σ_{ϕ_y}	3.1416	3.1416	6.3124
Γ	0	0	.6225

These results are then plotted alongside theory and simulation. Both experiments and corresponding simulations were conducted using $5,000$ realizations of uncorrelated random phase screens. This number was chosen as it provided a good threshold for a converged stabilized solution. Correlation results are referenced with respect to the center point.

Finally, although beam parameters differ between Ref. [9], a comparison is made between Stokes and irradiance correlation measurements to emphasis the reduction in registration errors.

4.1. Experiment I

Figure 4 shows the normalized observation Stokes parameters S_0 and S_1 of the experimental results compared to theory and simulation, in addition to the normalized DoP. The images are organized such that theory, simulation, and experiment appear in the columns left to right—theoretical results are Figs. 4(a), 4(d), and 4(g); simulation results are Figs. 4(b), 4(e), and 4(f); and experimental results are Fig. 4(c), 4(f), and 4(i). The rows are arranged as S_0, S_1, and DoP, respectively.

All three measurements agree nicely and match very well compared with theory. The DoP in Fig. 4(g) shows that there are polarimetric changes across the EGSM

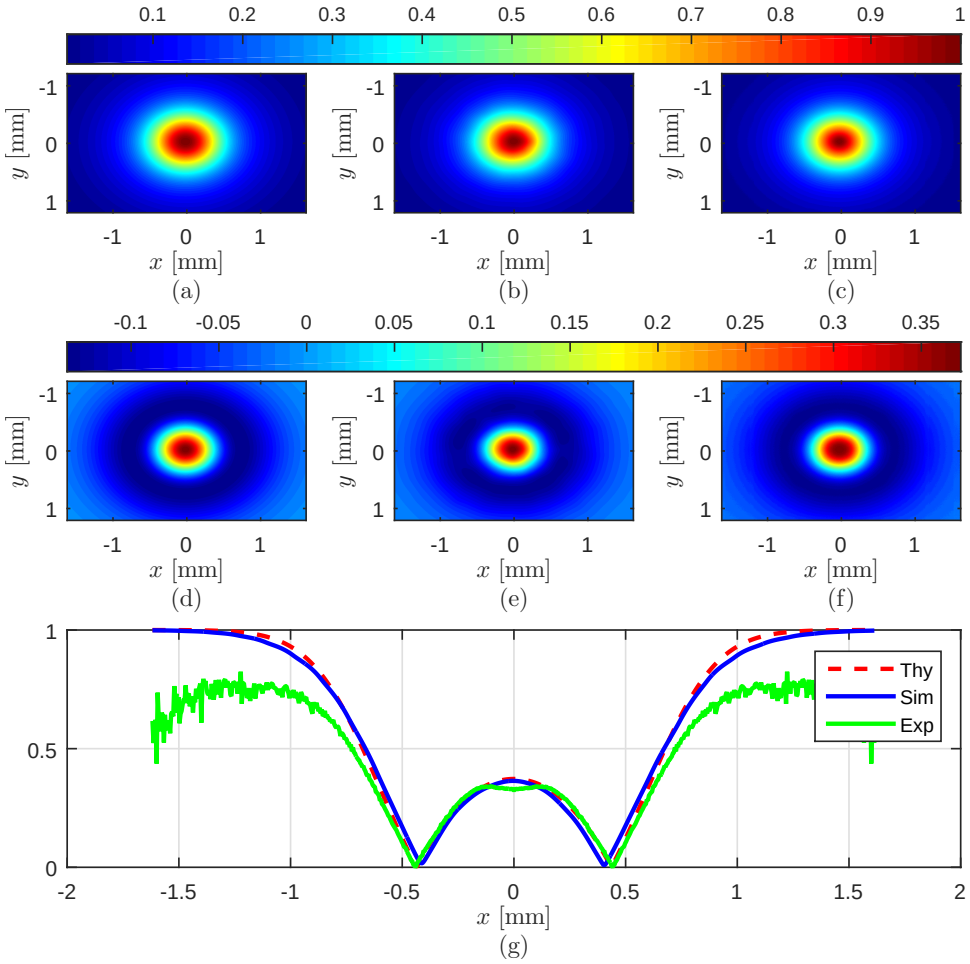

Figure 4. The columns are normalized observation Stokes theory, simulation, and experimental results, respectively; the rows are normalized S_0, S_1, and DoP, respectively.

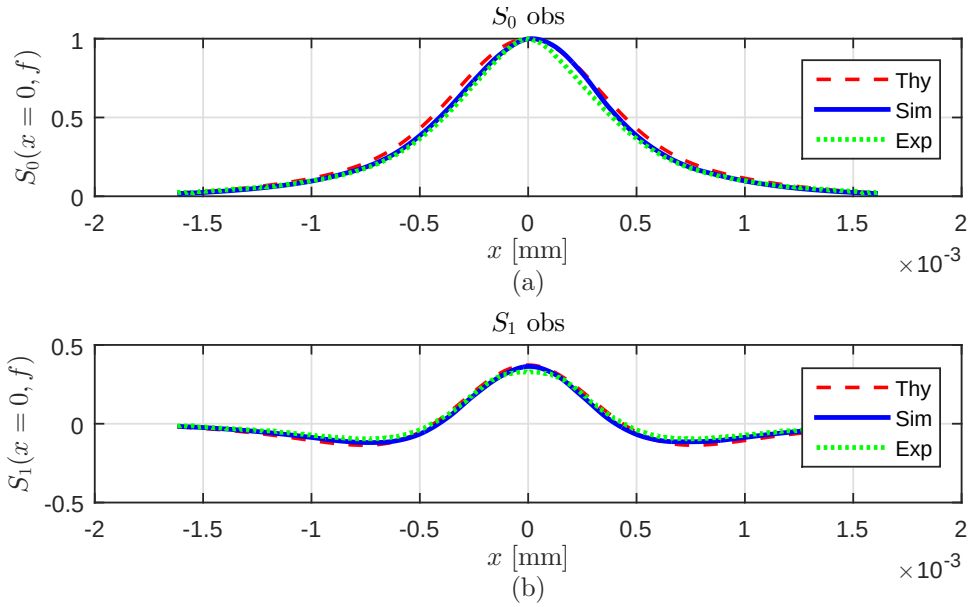

Figure 5. The rows $y = 0$ slice of S_0 and S_1 theory, simulation, and experiment results.

beam as it propagates. It is also consistent with theory and simulation. The lower and noisier tails for the experimental DoP are attributed to division by small numbers when normalizing results and the noise floor of the detector. Figure 5(a), further conveys the polarimetric change as the beam profile transitions between linear polarization states. As desired, S_1 in Fig. 5(b) shows polarization transitions back and forth between horizontal and vertical polarizations. Much of the polarization is influenced by the strength of the phase screens and their respective coherence parameters δ_{xx} and δ_{yy}. This is further influenced by the spectral density parameters in the source plane.

Figures 6(a)–(j) show the normalized irradiance correlations of theoretical, simulation, and center radial averaged experimental images with respect to the center point. The results show very good correlation and coherence control across the beam with the new amplitude control method. Figures 7(a)–(d) conveys this more which show $y = 0$ irradiance correlation with respect to the center point of theory, simulation, and experimental values. The rows are arranged $\langle I_x(x,y)I_x(0,0)\rangle$, $\langle I_x(x,y)I_y(0,0)\rangle$,

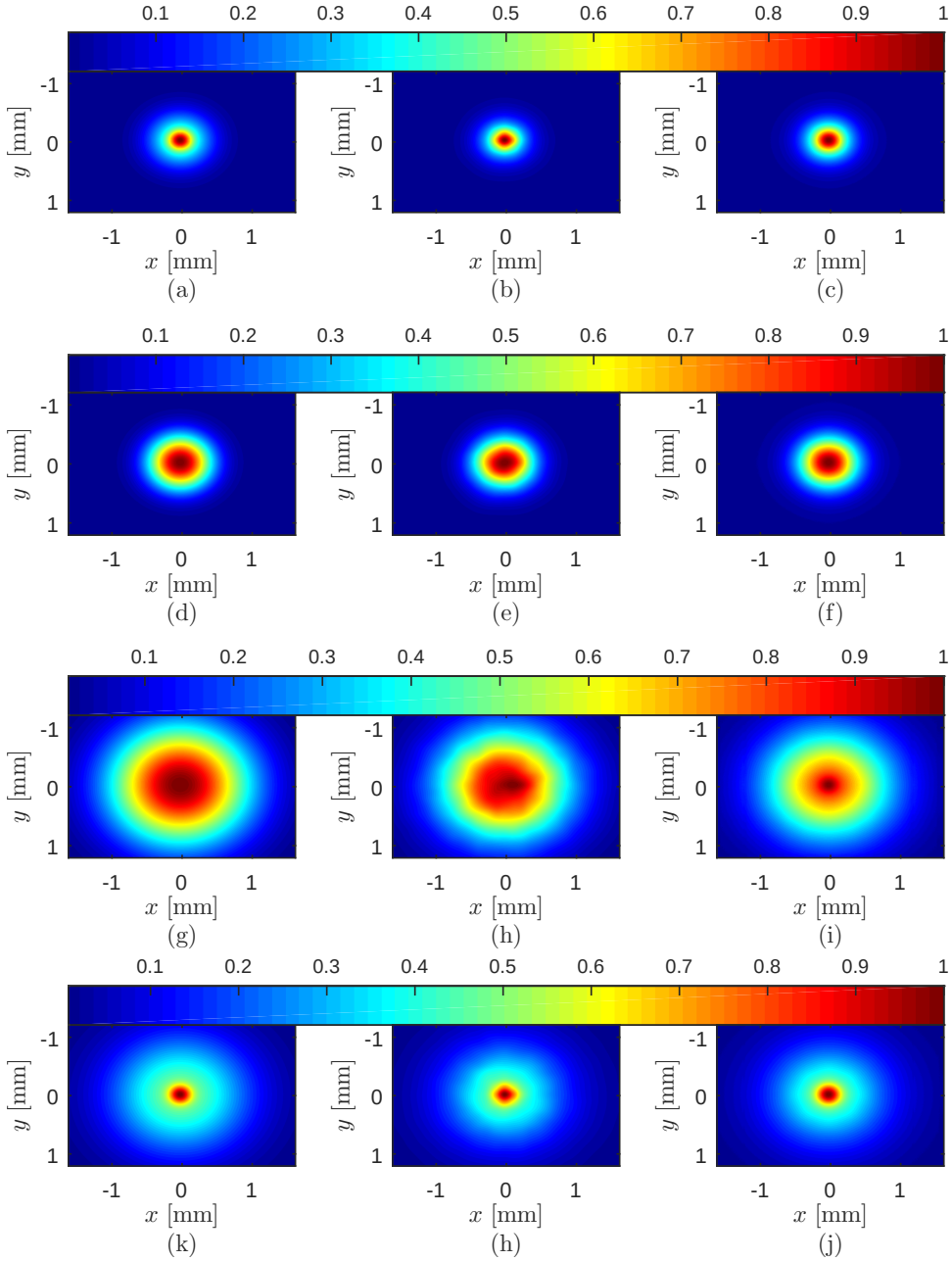

Figure 6. Experiment I correlation functions simulation and theory. The rows are $\langle I_x(x,y)I_x(0,0)\rangle$, $\langle I_x(x,y)I_y(0,0)\rangle$, $\langle I_y(x,y)I_x(0,0)\rangle$, and $\langle I_y(x,y)I_y(0,0)\rangle$ respectively, while the columns are the theory, simulation, and experiment, respectively.

$\langle I_y(x,y)I_x(0,0)\rangle$, and $\langle I_y(x,y)I_y(0,0)\rangle$, respectively.

With the exception of Fig. 7(a),(b), and (d), experimental data for Fig. 7(c) is not Gaussian as theory and simulation predict. Further investigation showed that I_y experimental data was not Gaussian and was influenced by some anomaly that is under further investigation. Since the SLM was not simulated, this could be a reason for the error. Another hypothesis has to do with the amplitude grating on the SLM. In simulation and theory, the Gaussian amplitude is created by each simulated pixel of the SLM, meaning both phase and amplitude are controlled on a per pixel basis. With the experiment, phase is controlled per pixel, but amplitude is controlled by a super pixel. This mismatch in sampling the field correctly is another area to investigate.

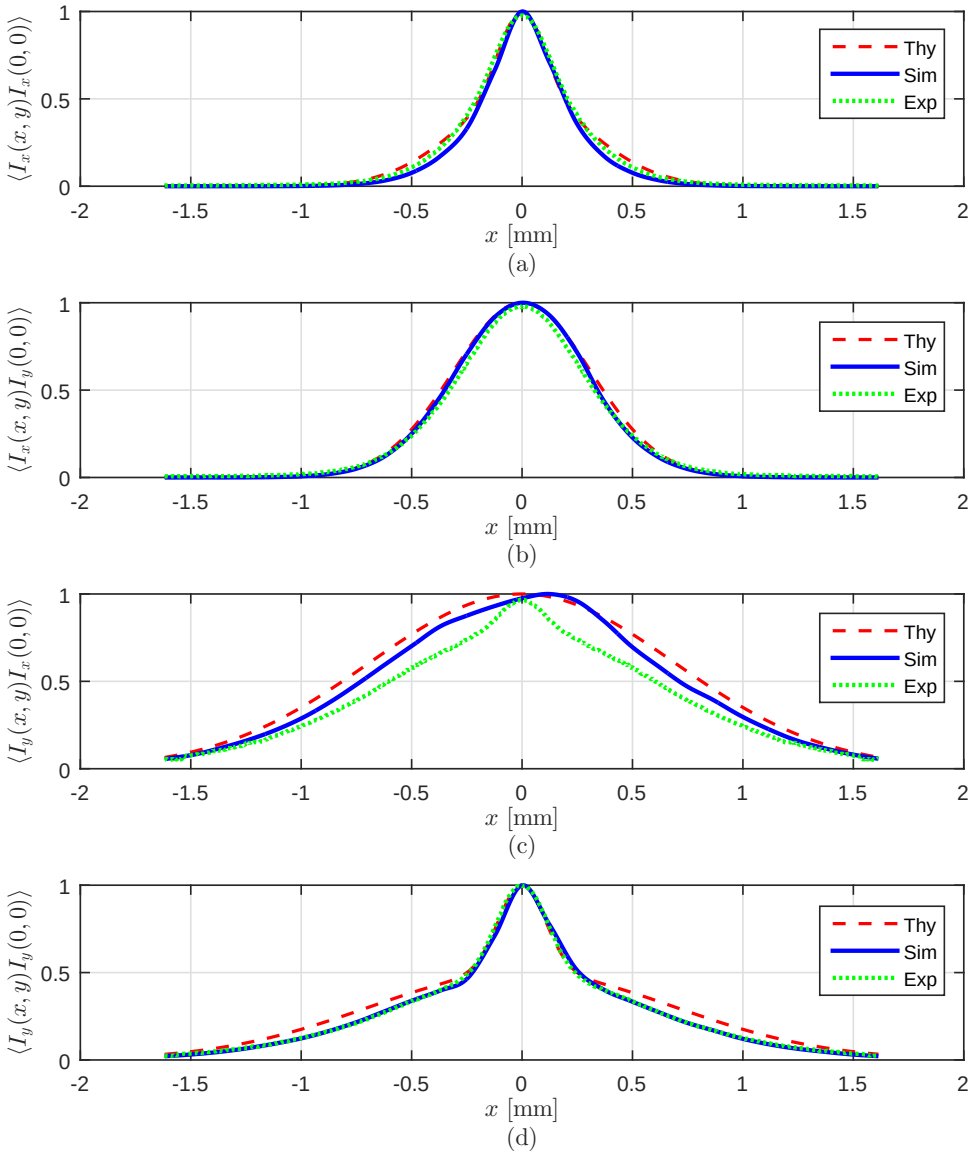

Figure 7. Experiment I irradiance correlation results along $x = 0$ with respect to the center point $(0, 0)$ compared with theory and simulation. The rows are $\langle I_x I_x \rangle$, $\langle I_x I_y \rangle$, $\langle I_y I_x \rangle$, and $\langle I_y I_y \rangle$, respectively.

4.2. Experiment II

Figure 8 shows the normalized Stokes parameter intensities S_0 and S_1 theory, simulation, and centered radially averaged experiment results. The images are organized such that theory, simulation, and experimental appear in the columns left to right– theoretical results are Figs. 8(a), 8(d), and 8(g); simulation results are Figs. 8(b), 8(e), and 8(f); and experimental results are Fig. 8(c), 8(f), and 8(i). The rows are arranged S_0, S_1, and DoP, respectively.

Experimental results show very good agreement with theory and simulation. The desired polarimetric change for S_1 can be seen as the beam transitions from horizontal to vertical polarization across the profile. This is supported by Figs. 9. As with Experiment I, the lower and noisier tails for the experimental DoP are attributed to division by small numbers when normalizing results and the noise floor of the detector.

Figure 10 shows the normalized irradiance correlation theoretical, simulation, and centered radially averaged experimental images with respect to the center point. The results show very good correlation and coherence control across the beam with the new amplitude control method. This is further supported by Fig. 11 which shows $y = 0$ slice irradiance correlation with respect to the center point of theory, simulation, and experimental values. The rows are arranged $\langle I_x(x,y)I_x(0,0)\rangle$, $\langle I_x(x,y)I_y(0,0)\rangle$, $\langle I_y(x,y)I_x(0,0)\rangle$, and $\langle I_y(x,y)I_y(0,0)\rangle$, respectively.

The boxing effect that in seen is Fig. 10(f) is due to the radial averaging and centering that takes place prior to the correlation process. Finally, experimental results show a predicted Gaussian profile for the cross correlation figures. The slightly lower experimental profile as seen in Fig. 11(c) is due to the fact the maximum of I_x remains slightly off axis and off center. As a result, the normalized measurements do not peak at one when using the $y = 0$ slice.

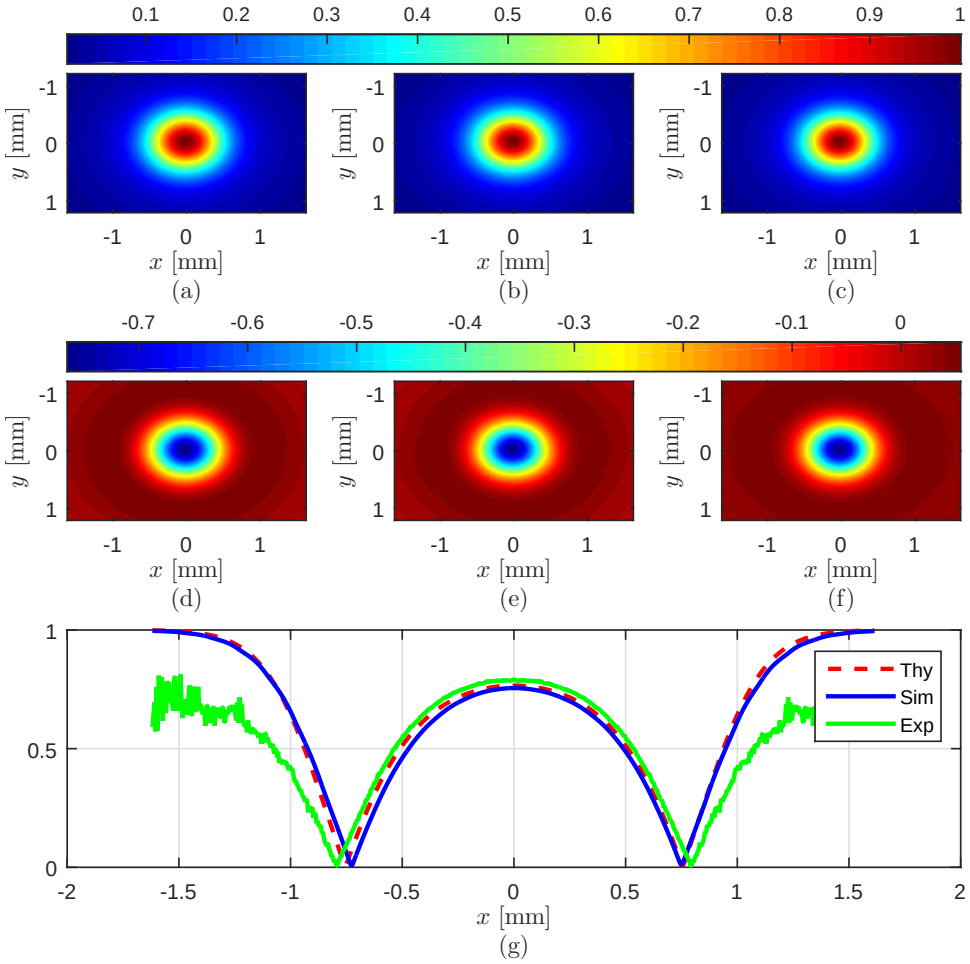

Figure 8. The columns are normalized observation Stokes theory, simulation, and experimental results, respectively; the rows are normalized S_0, S_1, and DoP, respectively.

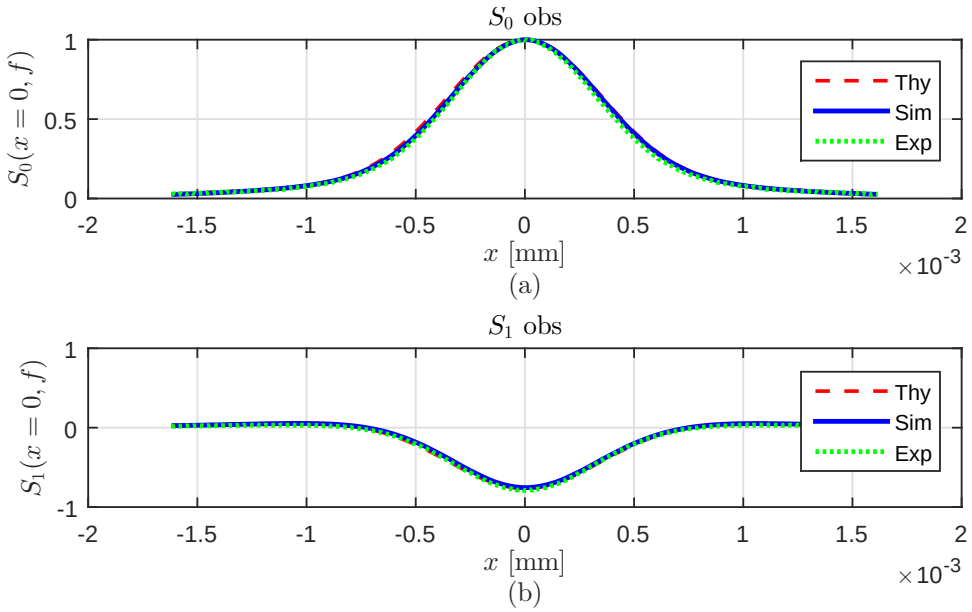

Figure 9. The rows are $y = 0$ slice of S_0 and S_1 theory, simulation, and experiment results.

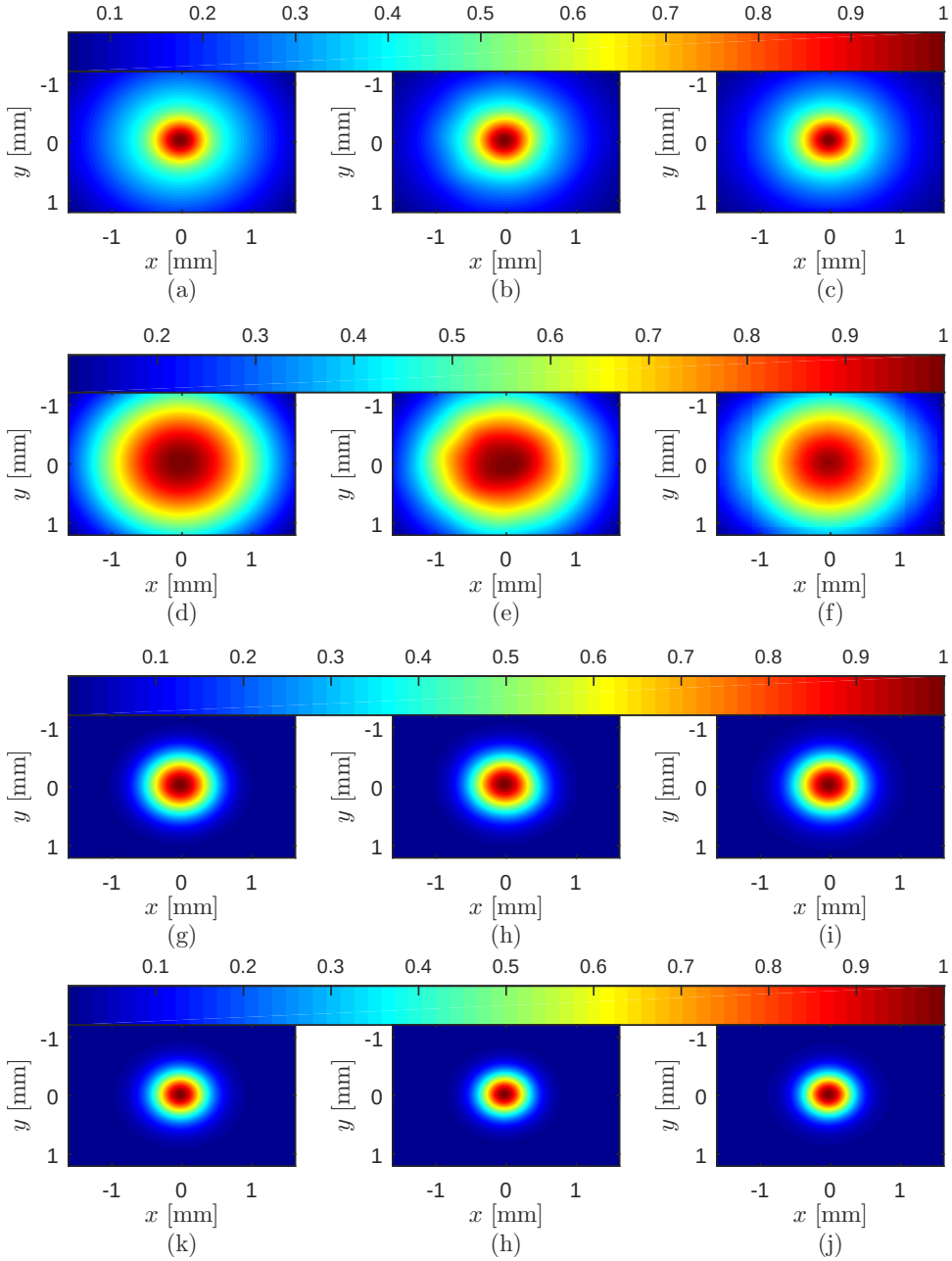

Figure 10. Experiment II correlation functions compared with simulation and theory. The rows are $\langle I_x(x,y)I_x(0,0)\rangle$, $\langle I_x(x,y)I_y(0,0)\rangle$, $\langle I_y(x,y)I_x(0,0)\rangle$, and $\langle I_y(x,y)I_y(0,0)\rangle$ respectively, while the columns are the theory, simulation, and experiment, respectively.

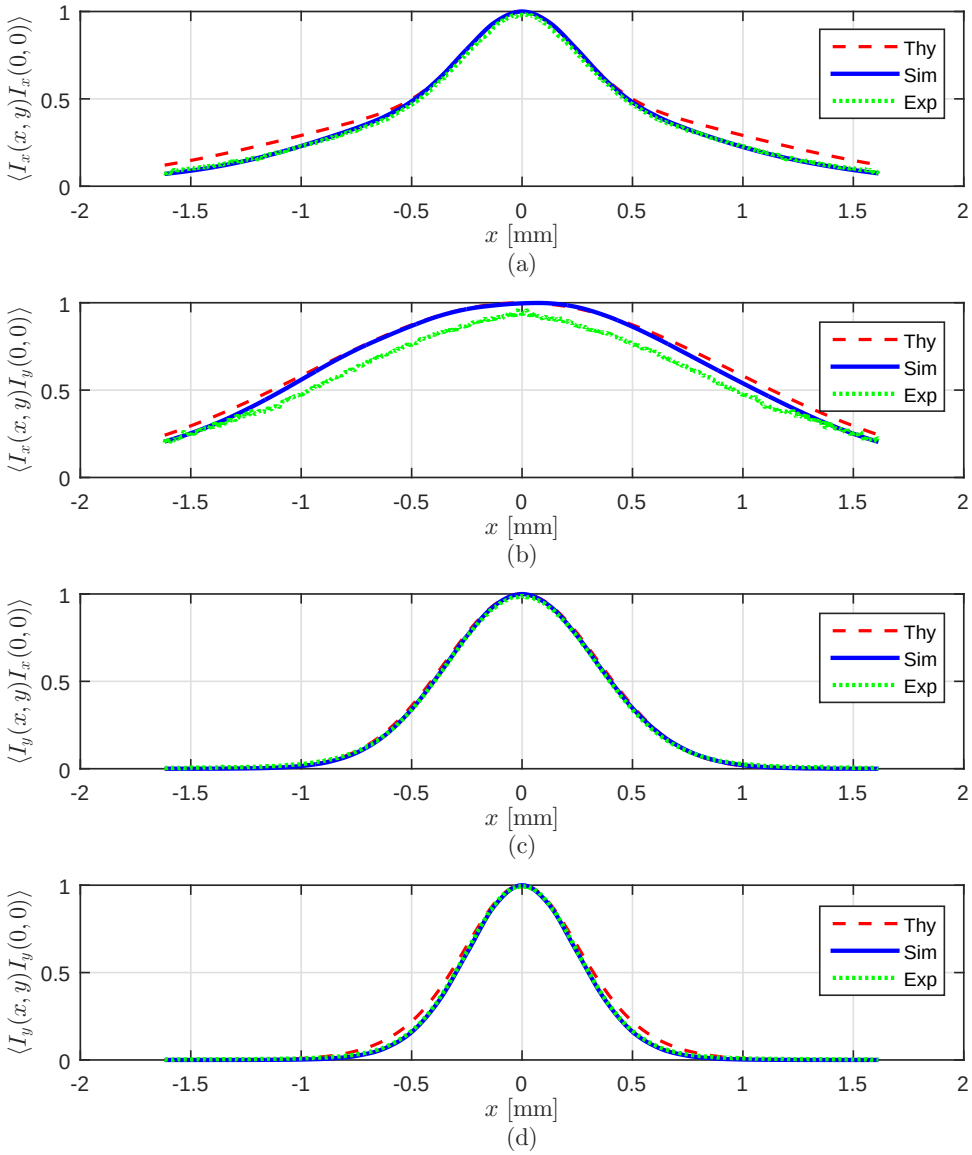

Figure 11. Experiment II irradiance correlation results along $x = 0$ with respect to the center point $(0, 0)$ compared with theory and simulation. The rows are $\langle I_x I_x \rangle$, $\langle I_x I_y \rangle$, $\langle I_y I_x \rangle$, and $\langle I_y I_y \rangle$, respectively.

4.3. Experimental Results Compared

The same measurements presented in Experiment I and II of this research were also presented in the Ref. [9]. The following Stokes and irradiance correlation figures from Experiment II in Ref. [9], as well as the experimental set-up are reproduced here for a qualitative and quantitative comparison. In Ref. [9], amplitude was controlled by a fixed Gaussian amplitude filter (GAF) optical element, Stokes parameters were calculated using calibration optical elements that required mechanical reset for each measurement, and experimental and simulation results were calculated using 1,000 realizations instead of 5,000. Source beam parameters from Ref. [9] were not reproduced using the SLM amplitude control due to the spatial extent limitations of the SLM and that of the GAF. Figure 12 shows the lab bench set-up that was used in Ref. [9]. Figure (b) and (c) expand Path 1 and Path 2 to reflect the two 4-f systems present in each leg. Since the new method of controlling amplitude is done using the SLM, there is no need for the second 4-f systems labeled LS2, LS4, or the GAFs.

Figure 13 shows Stokes parameters S_0 and S_1. Comparing Fig. 13 results to Fig. 5 and Fig. 9, it can be seen that the experimental data from Ref. [9] is not centered and shows some distortion on S_0. In addition, S_1 experimental data is highly corrupted and both simulation and experimental data do not match theory. Since Stokes parameters in Ref. [9] were calculated using calibrated instruments that required mechanical placement to measure I_x on the first iteration, then I_y on the second iteration, registration errors were introduced into the calculations. This resulted in a measurement that did not capture a pure single instance of both irradiances; an issue that was fixed with the new setup presented in Fig. 1.

Figure 14 shows the irradiance correlations for Experiment II in Ref. [9] along the slice $x = 0$. Experimental measurements are very distorted due to registration errors introduced during Stokes measurements. In addition, experimental results were not

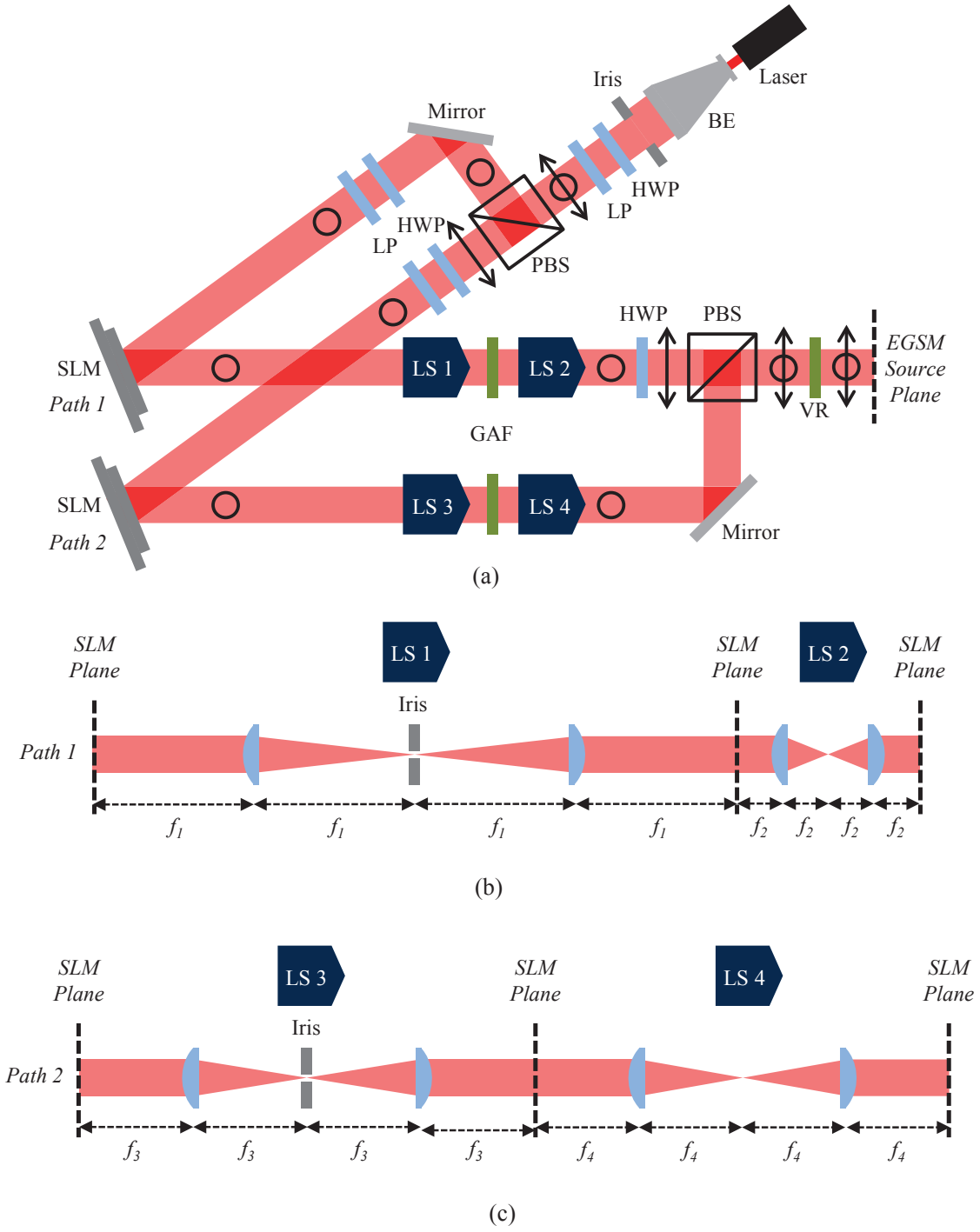

Figure 12. Subfigure (a) shows experimental set-up used in Ref. [9]. Subfigures (b) and (c) expand Path 1 and Path 2 into two 4-f systems with GAFs that control amplitude.

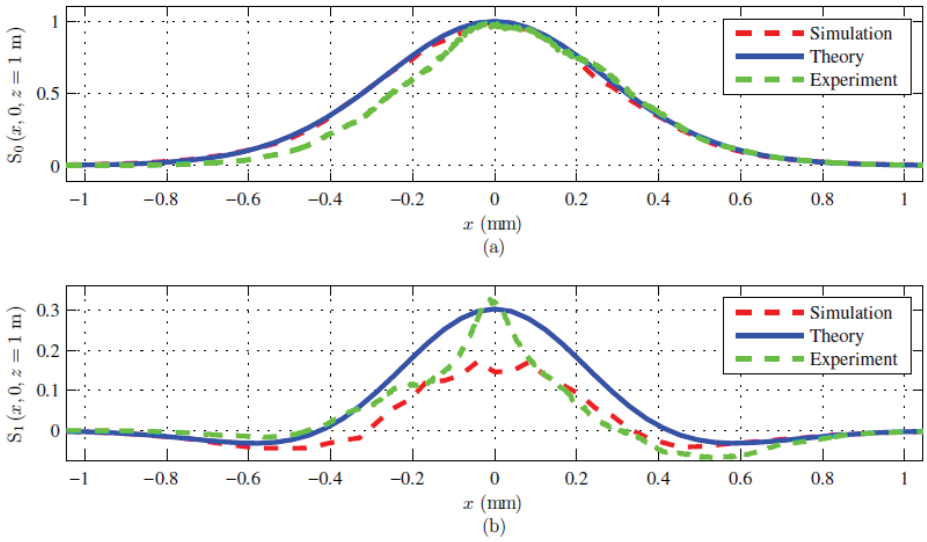

Figure 13. Stokes parameters at $x = 0$ slice of S_0 and S_1. The rows are S_0 and S_1 theory, simulation, and experiment results.

centered radially averaged when compared to simulation and theory.

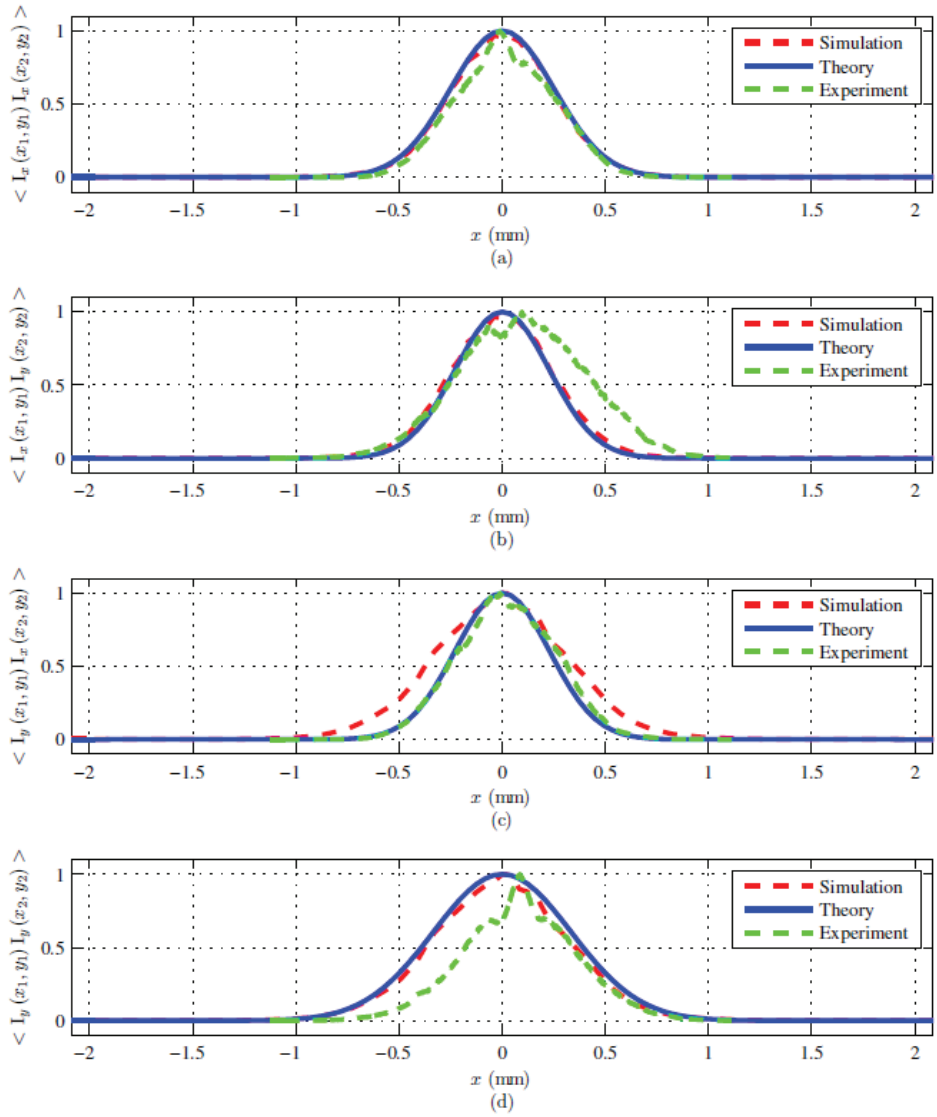

Figure 14. Experiment II irradiance correlation results along $x = 0$ with respect to the center point $(0, 0)$ compared with theory and simulation. The rows are $\langle I_x I_x \rangle$, $\langle I_x I_y \rangle$, $\langle I_y I_x \rangle$, and $\langle I_y I_y \rangle$, respectively.

V. Conclusion

Two experimental EGSM beams were made using a new method which significantly improved upon the research and findings in Ref. [9]. Implementation of the new amplitude grating control was successful and showed a range of dynamic control not previously achievable. In addition, registration errors were reduced, if not eliminated, due to the elimination of mechanical optical elements and having one camera measure both irradiance patterns. Finally, there was a reduction in the optical train footprint by removing two GAFs, two 4-f systems, one QWP, one LP, and one VR for a total of 9 optical elements.

Stokes parameters and correlation results matched very nicely for both experiments. Both beams exercised different source properties to achieve a desired EGSM in the observation plane which the results confirm. Overall this experiment was a success despite the limitations of not being able to measure S_2 and S_3.

Adding a turbulence model to the simulation and experiment would help further expand the understanding of how the desired EGSM parameters hold in a non vacuum environment. Another area of interest would be to develop alternative methods for measuring S_2 and S_3. Through a brain storming session, two such methods were discussed and both can be found in Section 5.1: Measuring S_2 and S_3. The first method involved the construction of a feedback interferometer system that would compensate for the random OPD differences. This would remove the random fluctuations allowing S_2 and S_3 to be measured directly. The second method discussed is to create a set-up that makes a common path for E_x and E_y.

This research and past research only focused mostly on Gaussian-Schell model sources that use Gaussian random phase screen and coherence functions. There are other Schell model sources that can be made, but using Gaussian phase screens to create non-Gaussian correlation functions at the source creates issues. References

[1, 11] explore using complex phase screens to create any partially coherent source such as electro-magnetic Bessel-Gaussian Schell model beams (EBGSM). Thus, there is much future work that can be done using the approach presented in this thesis.

5.1. Measuring S_2 and S_3

5.1.1 3-Bin algorithm.

The first method to help control the path lengths and ultimately S_2 and S_3, is to construct a 3-Bin interferometer [10, 19]. A feedback control loop is built that commands a variable retarder (VR). For this discussion, a 3-Bin algorithm is implemented as seen in Fig. 15 using independent legs for each phase bias. A phase retarder could also be used as a substitute for all three legs, where phase is cycled over a range of desired phase bias values. Each leg represents a different amount of phase delay ϕ_k. The mirrors are used to spatially offset each leg onto the camera where a linear polarizer set to 45° after the lens is used to create an interference irradiance pattern by picking of the common components between each polarization. For the calculations to follow, the BS are assumed to split power by 50/50; the scaling will be different if another power ratio for the BS are used. The following design will result in three measurements being taken simultaneously. To calculate the phase difference ϕ which represents the path difference, let ϕ_k represent the phase bias applied to each leg where $k = 0, 1, 2$ and $\phi_0 = 0$, $\phi_1 = \pi/2$, and $\phi_2 = \pi$. For the m_0 leg,

$$m_0 = \frac{1}{16}A_x^2 + \frac{1}{16}A_y^2 + \frac{1}{8}A_xA_y\cos(\phi + \phi_0) \tag{58}$$

Let $I_0 = \frac{1}{16}A_x^2 + \frac{1}{16}A_y^2$ and $I_1 = \frac{1}{8}A_xA_y$. Therefore,

$$m_0 = I_0 + I_1\cos(\phi) \tag{59}$$

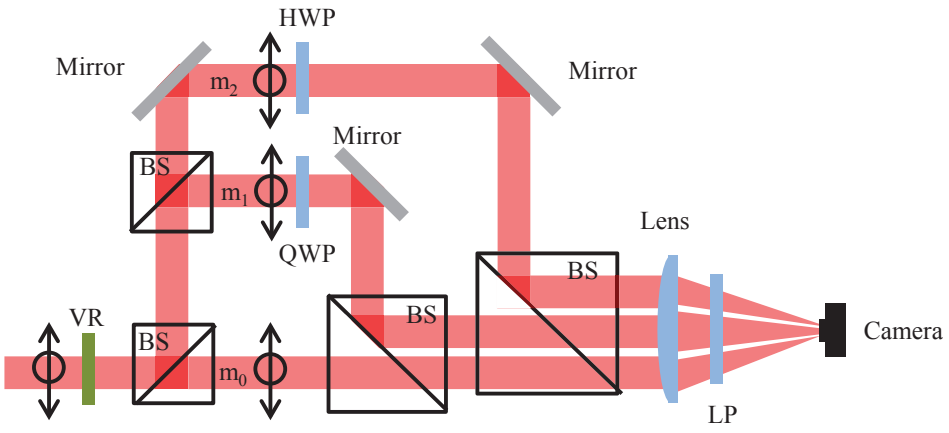

Figure 15. 3-Bin algorithm design for an interferometer to measure OPD for calculation of Stokes S_2 and S_3.

Using the above substitutions for I_0 and I_1,

$$\begin{aligned} m_1 &= \frac{1}{32}A_x^2 + \frac{1}{32}A_y^2 + \frac{1}{16}A_xA_y\cos(\phi+\phi_1) \\ &= \frac{I_0}{2} - \frac{I_1}{2}\sin(\phi) \\ m_2 &= \frac{1}{16}A_x^2 + \frac{1}{16}A_y^2 + \frac{1}{8}A_xA_y\cos(\phi+\phi_2) \\ &= I_0 - I_1\cos(\phi) \end{aligned} \tag{60}$$

This approach produces a system with three equations from which ϕ can be determined and controlled using a variable retarder. After reducing the linear system the following relation is used to find ϕ:

$$\phi = \text{atan}\left(\frac{m_0 + m_2 - 4m_1}{m_0 - m_2}\right) \tag{61}$$

During preliminary testing of this method, it was noted that the path length was varying faster than the refresh rate of the camera. It is recommended that a camera with at least 30 Hz or higher refresh rate is used.

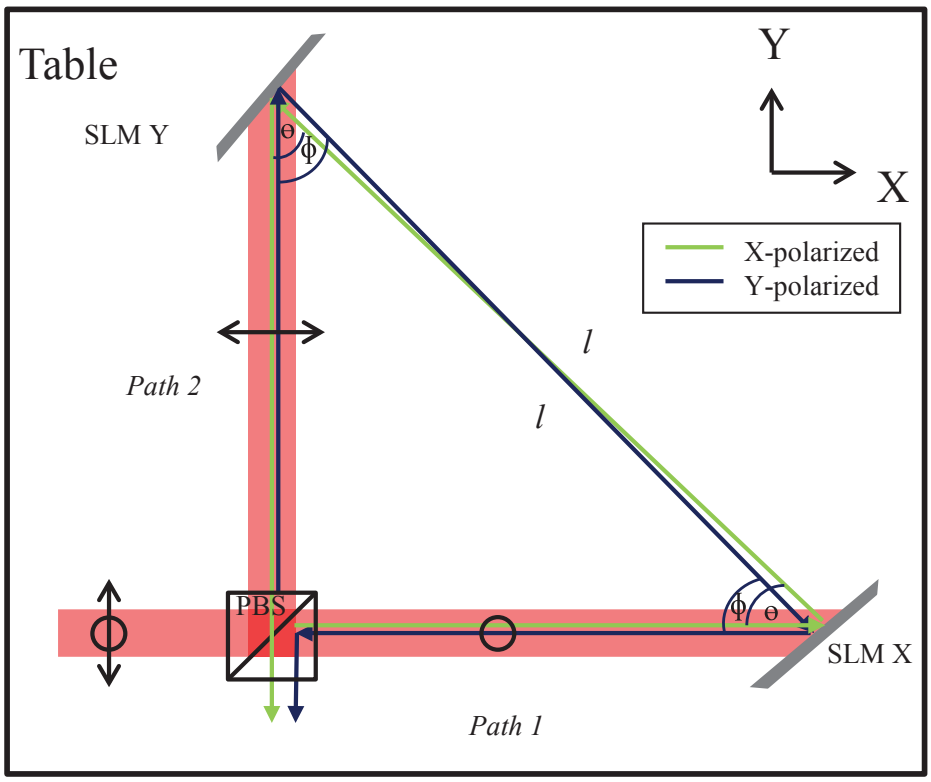

Figure 16. Configuration that shares a common path for the E_x and E_y field components.

5.1.2 Common path design.

Another method of trying to measure S_2 and S_3 is to implement a set-up where both E_x and E_y share a common path. This involves a triangular configuration shown in Fig. 16. The incoming beam is polarized at 45°. After entering a PBS, the vertical and horizontal components are separated and exit with the horizontal leg heading in the x direction and the vertical in the y direction with respect to the table layout. Since the SLMs only respond to vertically polarized light, the SLM on the horizontal leg must be rotated 90° to respond to the correct polarization. Referring to Path 1, the horizontally polarized light is incident on SLM-X. SLM-X commands the resultant beam into the first order. The horizontal beam is then reflected off the zeroth order of SLM-Y. The reflected beam then enters back into the PBS which now acts as a beam

combiner. Referring to Path 2, the vertically polarized light is incident on SLM-Y. SLM-Y commands the resultant beam into the first order. The vertical beam is then reflected off the zeroth order of SLM-X. Note that E_x and E_y transverse roughly the same path. For this configuration to work, θ and ϕ are approximately 45°. SLMs are not commonly operated at such high angles of incidence. Whether the SLMs will produce accurate E_x and E_y when operated under these conditions is unknown.

Bibliography

1. Avramov-Zamurovic, S., C. Nelson, S. Guth, O. Korotkova, and R. Malek-Madani. "Experimental study of electromagnetic Bessel-Gaussian Schell Model beams propagating in a turbulent channel". *Optics Communications*, 359:207 – 215, 2016. ISSN 0030-4018. URL http://www.sciencedirect.com/science/article/pii/S0030401815301553.

2. Basu, Santasri, Milo W. Hyde, Xifeng Xiao, David G. Voelz, and Olga Korotkova. "Computational approaches for generating electromagnetic Gaussian Schell-model sources". *Optics Express*, 22(26):31691–31707, Dec 2014. URL http://www.opticsexpress.org/abstract.cfm?URI=oe-22-26-31691.

3. Cai, Yangjian, Yahong Chen, and Fei Wang. "Generation and propagation of partially coherent beams with nonconventional correlation functions: a review". *Journal of the Optical Society of America*, 31(9):2083–2096, Sep 2014. URL http://josaa.osa.org/abstract.cfm?URI=josaa-31-9-2083.

4. Goldstein, D.H. *Polarized Light, Third Edition*. Taylor & Francis, 2010. ISBN 9781439830406. URL https://books.google.com/books?id=qi1JQgAACAAJ.

5. Goodman, Joseph W. *Introduction to Fourier Optics*. McGraw-Hill, San Francisco, 1968.

6. Goodman, Joseph W. *Statistical Optics*. Wiley, New York, 1985.

7. Gori, F., M. Santarsiero, R. Borghi, and V. Ramírez-Sánchez. "Realizability condition for electromagnetic Schell-model sources". *Journal of the Optical Society of America*, 25(5):1016–1021, May 2008. URL http://josaa.osa.org/abstract.cfm?URI=josaa-25-5-1016.

8. Gori, F, M Santarsiero, G Piquero, R Borghi, A Mondello, and R Simon. "Partially polarized Gaussian Schell-model beams". *Journal of Optics A: Pure and Applied Optics*, 3(1):1, 2001. URL http://stacks.iop.org/1464-4258/3/i=1/a=301.

9. Gridley, Matthew. *Experimental Method of Generating Electromagnetic Gaussian Schell-Model Beams*. Master's thesis, Air Force Institute of Technology, 2015.

10. Hardy, J.W. *Adaptive Optics for Astronomical Telescopes*. Oxford series in optical and imaging sciences. Oxford University Press, 1998. ISBN 9780195090192. URL https://books.google.com/books?id=-0aAWyckS_8C.

11. Hyde, Milo W. *Phase-Only Implementation of the Complex Screen Technique for Generating Schell-Model Sources*. Technical report, 2015.

12. Hyde, Milo W., Santasri Basu, David G. Voelz, and Xifeng Xiao. "Experimentally generating any desired partially coherent Schell-model source using phase-only control". *Journal of Applied Physics*, 118(9):093102, 2015. URL `http://scitation.aip.org/content/aip/journal/jap/118/9/10.1063/1.4929811`.

13. James, Daniel F. V. "Change of polarization of light beams on propagation in free space". *Optics Society of America*, 11(5):1641–1643, May 1994. URL `http://josaa.osa.org/abstract.cfm?URI=josaa-11-5-1641`.

14. Korotkova, Olga. *Random Light Beams : Theory and Applications*. CRC Press, 6000 Broken Suound Parkway NW, Suite 300, 2014.

15. Ostrovsky, Andrey S., Gustavo Rodríguez-Zurita, Cruz Meneses-Fabián, Miguel Á. Olvera-Santamaría, and Carolina Rickenstorff-Parrao. "Experimental generating the partially coherent and partially polarized electromagnetic source". *Optics Express*, 18(12):12864–12871, Jun 2010. URL `http://www.opticsexpress.org/abstract.cfm?URI=oe-18-12-12864`.

16. Roychowdhury, Hema and Olga Korotkova. "Realizability conditions for electromagnetic Gaussian Schell-model sources". *Optics Communications*, 249(4-6):379 – 385, 2005. ISSN 0030-4018. URL `http://www.sciencedirect.com/science/article/pii/S0030401805000957`.

17. Schmidt, Jason. *Numerical Simulation of Optical Wave Propagation*. SPIE, Bellingham, WA, 2010.

18. Schott, J.R. *Fundamentals of Polarimetric Remote Sensing*. SPIE tutorial texts. SPIE, 2009. ISBN 9780819478764. URL `https://books.google.com/books?id=-2V0gAJ3aG4C`.

19. Soloviev, OA. *Methods and sensors for accurate wavefront measurements*. Ph.D. thesis, TU Delft, Delft University of Technology, 2006.

20. Voelz, David G. *Computational Fourier Optics: A MATLAB Tutorial*. SPIE Press, Bellingham, WA, 2011.

21. Wang, Fei, Gaofeng Wu, Xianlong Liu, Shijun Zhu, and Yangjian Cai. "Experimental measurement of the beam parameters of an electromagnetic Gaussian Schell-model source". *Optics Letter*, 36(14):2722–2724, Jul 2011. URL `http://ol.osa.org/abstract.cfm?URI=ol-36-14-2722`.

22. Wolf, Emil. *Introduction to the Theory of Coherence and Polarization of Light*. Cambridge University Press, Cambridge, 2007.

23. Xiao, Xifeng and David Voelz. "Wave optics simulation approach for partial spatially coherent beams". *Optics Express*, 14(16):6986–6992, Aug 2006. URL `http://www.opticsexpress.org/abstract.cfm?URI=oe-14-16-6986`.

REPORT DOCUMENTATION PAGE

Form Approved
OMB No. 0704–0188

1. REPORT DATE *(DD–MM–YYYY)*	2. REPORT TYPE	3. DATES COVERED *(From — To)*
24–03–2016	Master's Thesis	Sept 2014 — Mar 2016

4. TITLE AND SUBTITLE

Using Phase Screens To Synthesize
Electromagnetic Gaussian-Schell Model Sources
With Desired Amplitude, Coherence, and Polarization

5a. CONTRACT NUMBER

5b. GRANT NUMBER

5c. PROGRAM ELEMENT NUMBER

6. AUTHOR(S)

Kokoczka, Christopher J., Captain, USAF

5d. PROJECT NUMBER

ENGJON15G209

5e. TASK NUMBER

5f. WORK UNIT NUMBER

7. PERFORMING ORGANIZATION NAME(S) AND ADDRESS(ES)

Air Force Institute of Technology
Graduate School of Engineering and Management (AFIT/EN)
2950 Hobson Way
WPAFB OH 45433-7765

8. PERFORMING ORGANIZATION REPORT NUMBER

AFIT-ENG-MS-16-M-026

9. SPONSORING / MONITORING AGENCY NAME(S) AND ADDRESS(ES)

Air Force Office of Scientific Research
2950 Hobson Way
WPAFB OH 45433-7765
COMM 703-696-9586
Email: Julie.moses@us.af.mil

10. SPONSOR/MONITOR'S ACRONYM(S)

AFOSR/RTB

11. SPONSOR/MONITOR'S REPORT NUMBER(S)

12. DISTRIBUTION / AVAILABILITY STATEMENT

DISTRIBUTION STATEMENT A:
APPROVED FOR PUBLIC RELEASE; DISTRIBUTION UNLIMITED.

13. SUPPLEMENTARY NOTES

The views expressed in this document are those of the author and do not reflect the official policy or position of the United States Air Force, the United States Department of Defense or the United States Government. This material is declared a work of the U.S. Government and is not subject to copyright protection in the United States.

14. ABSTRACT

An electromagnetic Gaussian-Schell model (EGSM) source is built with desired coherence, amplitude, and polarization using correlated phase screens based on research conducted in Refs. [2, 9]. A new method of amplitude control is presented and tested using spatial light modulators (SLM). A brief review of theory and concepts is discussed followed by methods of how to build an EGSM source, correlated phase screens, and control amplitude using SLM gratings. The experimental set-up is presented which builds EGSM sources that demonstrate desired amplitude, coherence, and polarization. Correlation, degree of polarization, and Stokes parameters S_0 and S_1 are examined and compared to theoretical predictions to validate experimental results. The results are summarized and future work is discussed including methods of calculating and measuring Stokes S_2 and S_3.

15. SUBJECT TERMS

electromagnetic Gaussian-Schell model, EGSM, GSM, partially coherent, partially polarized, amplitude grating, SLM, spatial light modulator, first order, phase screen, Stokes

16. SECURITY CLASSIFICATION OF:			17. LIMITATION OF ABSTRACT	18. NUMBER OF PAGES	19a. NAME OF RESPONSIBLE PERSON
a. REPORT	b. ABSTRACT	c. THIS PAGE			Maj Milo W. Hyde IV, PhD AFIT/ENG
U	U	U	U	65	19b. TELEPHONE NUMBER *(include area code)* (937) 255-3636, x4371; Milo.Hyde@afit.edu